4polar-STORM polarized super-resolution imaging of actin filament organization in cells

Caio Vaz Rimoli, Cesar Augusto Valades Cruz, Valentina Curcio, Manos Mavrakis, Sophie Brasselet

4polar-STORM polarized super-resolution imaging of actin filament organization in cells

Caio Vaz Rimoli[1,&], Cesar Augusto Valades Cruz[2,3,&], Valentina Curcio[1], Manos Mavrakis[1,*], Sophie Brasselet[1,*]

1 Aix Marseille Univ, CNRS, Centrale Marseille, Institut Fresnel, F-13013 Marseille, France

2 Institut Curie, PSL Research University, UMR144 CNRS, Space-Time imaging of organelles and Endomembranes Dynamics Team, F-75005, Paris, France

3 Inria Centre Rennes-Bretagne Atlantique, SERPICO Project Team, F-35042, Rennes, France

[&] these authors contributed equally to the work

* corresponding authors contact : sophie.brasselet@fresnel.fr, manos.mavrakis@univ-amu.fr

Abstract

Advances in single-molecule localization microscopy are providing unprecedented insights into the nanometer-scale organization of protein assemblies in cells and thus a powerful means for interrogating biological function. However, localization imaging alone does not contain information on protein conformation and orientation, which constitute additional key signatures of protein function. Here, we present a new microscopy method which combines for the first time Stochastic Optical Reconstruction Microscopy (STORM) super-resolution imaging with single molecule orientation and wobbling measurements using a four polarization-resolved image splitting scheme. This new method, called 4polar-STORM, allows us to determine both single molecule localization and orientation in 2D and to infer their 3D orientation, and is compatible with high labelling densities and thus ideally placed for the determination of the organization of dense protein assemblies in cells. We demonstrate the potential of this new method by studying the nanometer-scale organization of dense actin filament assemblies driving cell adhesion and motility, and reveal bimodal distributions of actin filament orientations in the lamellipodium, which were previously only observed in electron microscopy studies. 4polar-STORM is fully compatible with 3D localization schemes and amenable to live-cell observations, and thus promises to provide new functional readouts by enabling nanometer-scale studies of orientational dynamics in a cellular context.

Introduction

Protein conformation and the precise way in which proteins arrange in space to form higher-order macromolecular assemblies are key elements of biological functions in cells and tissues. Adhesion of animal cells to the extracellular matrix is driven, for example, by dramatic conformational changes in force-sensing and force-transducing proteins such as integrins and talins. The precise geometry of actin filament assemblies[1,2,3,4,5] and its remodelling in space and time are further determinant for cell mechanics driving essential biological processes, including immune responses and tissue development. Thus, understanding the function of a protein and its interaction with its partners, necessitates that

we observe its organization at the nanometer scale, both in position and orientation. This need is shared by many fields in biology from immunology, neurobiology and mechanobiology, to developmental biology. Current methods reporting protein organization such as electron microscopy or X-ray diffraction are however not yet applicable to a live imaging context. Single molecule localization microscopy (SMLM) has brought considerable progress towards this goal, enabling imaging with a resolution down to tens of nanometers even in live cells[6,7,8,9]. However, while these methods report the localization of single molecules with high precision, they do not measure their orientation. If fluorophores are linked to the proteins of interest rigidly enough[10], reporting their orientation could provide precious information on the structural organization of the attached proteins and on their conformational behaviors, which is inherently missing in localization-based optical imaging methods. While measuring fluorophore orientation precisely and accurately is a challenge that is of high interest in the field of SMLM imaging, it is however a delicate task. First, it is necessary to not only measure their 3D orientation, averaged over the imaging time, but also the extent of their orientation fluctuations, which naturally occurs when fluorophores wobble at fast time scales[10] (Fig. 1a). A failure to uncouple their mean orientation from their fluctuations makes it impossible to determine accurately how the fluorophore-conjugated molecules are organized and can lead to misleading interpretations[10]. Second, orientation and spatial position are difficult to disentangle in SMLM, because of their intrinsic coupling in the process of the formation of their PSF image in a microscope[11,12]. The development of an optimal method to disentangle spatial position, mean orientation and orientation fluctuations is still an ongoing research[13]. One approach is to encode the orientation and wobbling information into the shape of the single molecules' point spread function (PSF), using custom-designed phase or birefringent masks[14,15,16]. This strategy comes however at the price of some constraints, which restrain its use in regular SMLM imaging. PSF engineering induces an increase of the PSF size, with the PSF shape including both orientation and wobbling information in an intricate way, limiting its use in densely-labelled structures. PSF engineering also involves practical and methodology difficulties due to complex data analysis procedures and stringent calibrations to avoid sources of bias such as optical aberrations. Along similar lines, exploiting un-engineered PSF shape changes due to image defocusing[17,18] or to the proximity of the molecule to the coverslip interface[19] has been proposed, however with similar limitations as encountered in PSF engineering. A less constraining approach is to use polarization projections of the image plane, and perform ratiometric intensity measurements between different polarization channels. Two-orthogonal polarization splitting has allowed fluorescence anisotropy measurements in isotropic environments[20] and used to quantify actin filament alignment in 2D[10], however with the inconvenience of an estimation ambiguity for fluorophore orientations symmetric relative to the polarization axes. Additionally, two-orthogonal polarization splitting does not efficiently decouple orientation from wobbling. Both ambiguities have been waived by the use of a four-polarization projection scheme[21,22,23,24]. A strong limitation still present in currently reported four-polarization split approaches is however that due to the high numerical apertures used, the intensities measured are strongly influenced by the off-plane 3D orientation of the fluorophores, resulting in large inaccuracies in the determination of their wobbling[23]. The failure to provide accurate measurements of fluorophore wobbling has precluded its use as an additional readout for protein organization. It is indeed conceivable that fluorophore wobbling is related to local packing constraints of the labelled protein. Importantly, single molecule studies using four polarizations projections have not yet been applied to super-resolution imaging and have so far been limited to situations employing

sparse labelling or/and photobleaching to obtain single fluorophores[21,22,23,24]. In this work, we combine for the first time Stochastic Optical Reconstruction Microscopy (STORM) super-resolution imaging with single molecule orientation and wobbling measurements using four-polarization image splitting in a new method called 4polar-STORM. 4polar-STORM imaging is compatible with high labelling densities and is thus ideally placed for the determination of the organization of dense protein assemblies in cells. 4polar-STORM imaging further uses a slightly reduced detection numerical aperture, allowing us to not only determine the 2D mean orientation and wobbling of fluorophores in a reliable way, but also to infer their 3D orientation and thus provide additional information on protein organization and function that is otherwise difficult to obtain.

With this new approach, we reveal the nanometric-scale structural organization of actin filaments inside dense actin filament-based structures involved in the adhesion and motility of cells, notably stress fibers (SFs) and lamellipodia. Actin is at the center of interest in the development of super-resolution imaging methods where so far, only localization-based images have been exploited[25,26,27,28,29,30]. Here we use 4polar-STORM imaging to quantify the orientational behaviour of fluorophores in single actin filaments used as a reference, and in fixed cells. We show that actin filaments are highly aligned in all types of SFs in cells, in line with EM studies[31,32], and further reveal that SFs contain not only 2D but also 3D oriented populations of actin filaments, whose nanometer-scale organization is consistent with the different proposed mechanisms for their assembly. Mild pharmacological inhibition of myosin II activity to relax contractile SFs, while keeping SFs macroscopically intact, led to a perturbation of the nanometric actin filament organization, as revealed by 4polar-STORM imaging, highlighting the dependence of contractile SF organization on Myosin II activity. Finally, 4polar-STORM imaging in the dense meshwork of the lamellipodium at the leading edge of motile cells revealed bimodal distributions of actin filament orientations, with non-negligible 3D oriented filament populations. Such bimodal orientation distributions have not been reported with other super-resolution light microscopy methods, to our knowledge, due to the high actin density in this area[25], and were previously only observed in EM studies of the lamellipodium[3,33,34,35,36]. This new method is amenable to live-cell observations, and promises to complement electron microscopy studies in cells, while allowing for nanometer-scale measurements of molecular organization in large (tens of micrometers) fields of views.

4polar-STORM imaging applied to actin filaments

Fluorophores attached to a protein act as emission dipoles. While their position is directly defined as the center of their PSF image, their orientation is not directly extractable. A fluorophore is represented by its mean orientation (ρ,η) averaged over the imaging integration time, and its wobbling angle (δ_{3D}) explored during this integration time (Fig. 1a). 4polar-STORM measures the fluorophore's orientation and wobbling projected in the sample plane (ρ,δ) (Fig. 1a) based on the projection of the fluorescence signal on four polarizations channels along the directions 0°, 45°, 90°, and 135° respectively (0° corresponding here to the horizontal direction of the sample) (Fig. 1b). The 4-polarization splitting approach leads to only a minor deformation and enlargement of the image PSF, affecting minimally the signal to noise ratio (SNR) and PSF complexity. In contrast to a 2-polarization projection[10], 4-polarization projection permits to waive coupling ambiguities and therefore to retrieve ρ and δ

independently. Supplementary Note 1 details the theoretical framework for the retrieval of the orientation parameters (ρ,δ). We note that δ is the sample-plane 2D projection of the wobbling cone angle δ_{3D}, it therefore differs from the real 3D wobbling value δ_{3D}. At large off-plane tilt angles in particular (small η angle in Fig. 1a), the projection of the wobbling cone angle is biased and δ is an overestimation of δ_{3D}. Theoretical calculations of the dependence of this bias on the detection numerical aperture (NA) and on the tilt angle of the fluorophore, show that a solution for minimizing this bias is to lower the NA to a value close to 1.2 (Supplementary Note 1). Even though both SNR and PSF size are expected to be slightly degraded for this lower NA, this permits to give a low-bias estimate of δ_{3D} with a reasonable compromise on the loss of signal, as long as the tilt angle of the fluorophore off-plane orientation η does not surpass 45° (Supplementary Note 1 and Fig. S1).

The retrieval of the orientation parameters (ρ,δ) consists in detecting first the 2D position of single molecules in each of the polarization channels, previously corrected for imperfections in the detection paths (Supplementary Note 2) and registered (Supplementary Note 3). Each molecule is associated to its pairs in all polarization channels, where polarized PSF amplitudes and sizes are deduced from a Gaussian fit in order to calculate intensities along each of the polarized channels (Fig. 1b) (Supplementary Note 3). We note that if molecules have a well-defined orientation and are oriented off-plane, their PSF will enlarge and deform towards a donut-shape[37]. Even though this effect is minimized when molecules wobble[38], the PSF fit has to allow for larger ranges of sizes, since the measured PSF size for tilted molecules can be larger than for in-plane molecules. Once intensities are determined in the four polarization channels, a retrieval calculation permits to extract both ρ and δ parameters per molecule (Supplementary Note 1). This calculation uses a relatively simple model, for computational speed reasons, which is shown to be very close to a complete model characterization accounting for the inversion of the propagation equations (Supplementary Note 1 and Fig. S2).

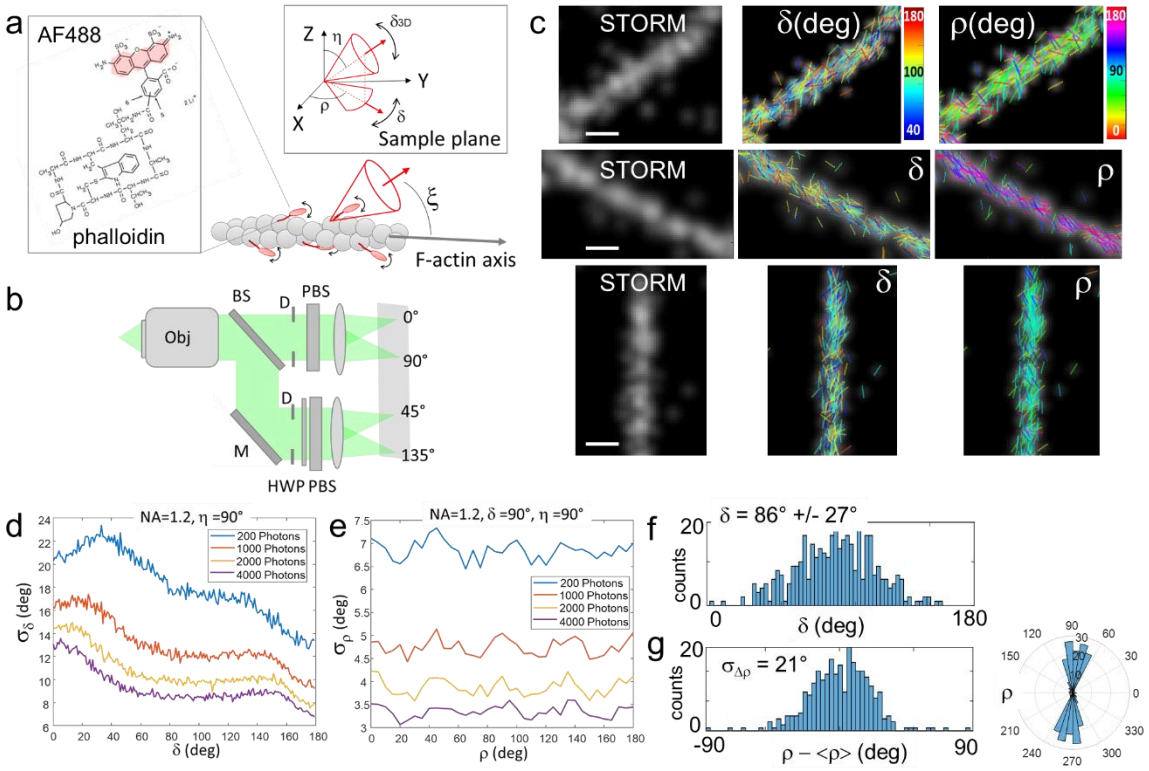

Figure 1. (a) Schematic representation of a wobbling Alexa Fluor 488 (AF488)-phalloidin conjugate labelling an actin filament (F-actin). The structure of the phalloidin conjugate is shown on the left, with the fluorophore moiety highlighted in red. (ρ,η) represent the mean orientation of a single fluorophore in 3D, with ρ the projected orientation in the sample plane (XY) and η its off-plane tilt angle with respect to the optical axis of the microscope (Z). δ_{3D} is the wobbling cone angle of the fluorophore in 3D, and δ its projection in the sample plane. ξ is the mean orientation of the fluorophore relative to the actin filament axis. (b) Schematic optical setup of 4polar-STORM imaging. BS, beam splitter; M, mirror; D, diaphragm; HWP, half-wave plate; PBS, polarizing beam splitter. (c) Examples of 4polar-STORM images of single AF488-phalloidin molecules labelling single actin filaments. Left panels depict single molecule localization STORM images (blurred using a Gaussian filter with a sigma of 0.3 pixel size). Middle and right panels depict single molecule wobbling (δ) and orientation (ρ) measurements overlaid with the STORM image depicted in grayscale. Each single molecule is represented as a stick whose orientation is ρ relative to the horizontal axis and whose color is the measured parameter (ρ or δ). Scale bars, 170 nm. (d) Monte Carlo simulations of the expected precision on δ under different signal level conditions (signal in photons, 1000 photons = 4.5x10^4 camera counts). 5000 realizations are used for η = 90° (in-plane molecules) in the presence of camera detection noise using the experimental conditions and a gain of 300 (the results do not depend on ρ) (see Supplementary Fig. S3). (e) Corresponding Monte Carlo simulations for the estimation of ρ precisions reached for (δ = 90°, η = 90°) (the results do not strongly depend on δ apart for $\delta = 0°$ and 180°). (f) Representative experimental δ histogram obtained on a straight segment of a single actin filament (see (c)). (g) Corresponding ρ histogram in both standard and polar-plot representations, depicting the distribution of orientation angle values relative to the average within the measured region of interest, $\Delta\rho = \rho - \langle\rho\rangle$. $\sigma_{\Delta\rho}$ is the standard deviation of $\Delta\rho$. For both histograms, intensities are thresholded above 5x10^4 camera counts and localization precisions are thresholded below 0.15 pixels (σ_{loc} < 20 nm).

Using the theoretical framework we established for the retrieval of orientation parameters, we aimed at using 4polar-STORM imaging to measure the nanometer-scale actin filament organization in complex assemblies in cells labelled with fluorophore-conjugated phalloidin molecules, which provide specific labelling of actin filaments[39,40]. Our measurements will allow us to extract both the degree of angular fluctuations of the fluorophores (δ angle in Fig. 1a), and their mean orientation in the sample plane (ρ angle in Fig. 1a). To evaluate the fluorophore orientation behaviour in a flat, single actin filament with a well-defined direction, we started by reconstituting single actin filaments immobilized on a glass surface (see Methods). This provides a reference for later deciphering actin filament organization in unknown, more complex assemblies. Figure 1c shows the results obtained on isolated actin filaments labelled with Alexa Fluor 488 (AF488)-phalloidin. Single AF488 molecules measured by 4polar-STORM are represented as sticks whose color is the wobbling angle δ and whose orientation, relative to the horizontal axis, is the angle ρ. Figure 1c shows that AF488 molecules are oriented along the actin filament axis, and exhibit a non-negligible degree of orientational flexibility δ. The expected precision on both ρ and δ, depicted in Fig. 1d,e, was evaluated by Monte Carlo simulations under different signal levels, accounting for the camera noise (Supplementary Figure S3). Typical measured total intensities from single molecules are around 5 to $10x10^4$ camera counts. At $5x10^4$ camera counts (e.g. 1100 photons), we expect an error of 12° for δ in the measured range of δ values (Fig. 1d), and of 5° degrees for ρ (Fig. 1e). This error decreases with the signal level and is expected to increase in the presence of background. In order to exclude degraded signal in 4polar-STORM due to background conditions, and provide high precision estimates, we systematically threshold the experimental data to a minimum intensity of $5x10^4$ camera counts, and to a maximum localization precision value σ_{loc} of 0.15 pixels (corresponding to 20 nm). Straight segments of actin filaments were selected under such conditions, and typical statistics obtained on δ and ρ in these regions are plotted in Fig. 1f and Fig. 1g respectively. Measurements of the orientation angles ρ are depicted relatively to the average $<\rho>$ over the molecules measured in the region of interest, $\Delta\rho = \rho - <\rho>$ (Fig. 1g). The distribution of $\Delta\rho$ is characterized by a standard deviation $\sigma_{\Delta\rho}$ which represents the range of orientations explored by single AF488 molecules with respect to the actin filament; $\sigma_{\Delta\rho}$ also gives a measurement of the fluorophore tilt angle with respect to the filament axis (ξ angle in Fig. 1a). Figures 1f,g show that AF488 labels are, on average, oriented along the actin filament direction with a tilt angle of about ξ = 20° with respect to the actin filament axis, and a non-negligible wobbling of δ = 85-90°. This is consistent with the fact that the phalloidin-fluorophore conjugate exhibits a very small size (on the order of 1 nm) and a structure that fits in the groove formed by three neighbouring G-actin monomers[41], while leaving some space for mobility for the fluorophore. As previous studies have suggested, this degree of mobility is expected to originate mostly from the structure of the fluorophore itself and its precise conjugation to the phalloidin moiety, AF488 being among the least wobbly fluorophores among STORM dyes[10].

Using the same labelling approach, we next investigated the organization of actin filaments in structures that are expected to be highly organized in cells, notably actin stress fibers (SFs). We focused on ventral stress fibers, both ends of which associate with focal adhesions (FAs) on the ventral surface of the cell; on dorsal stress fibers, with one end associating with FAs on the ventral surface and the other end extending upwards toward the dorsal cell surface; and on meshworks (Fig. 2a). A minimum intensity threshold of $5x10^4$ camera counts and a maximum localization precision value σ_{loc} of 0.15 pixels are applied to all data in order to exclude estimates that lead to low precision and inaccuracy in

the parameters' determination. 4polar-STORM images of an actin-stained cell are shown in Fig. 2b-d, which depict respectively the single molecule localization image (STORM), the ρ and the δ images from the same cell. In well isolated thin ventral SFs, AF488 is oriented predominantly along the SF direction (ROI 1 in Figs. 2e,f, with polar histograms of single molecule orientations shown as insets in f), similarly to what was observed in single actin filaments (Fig. 1). This observation confirms that these SFs are made of highly parallel filaments, which is expected from the tight crosslinking of these structures[3]. Many molecules exhibit however larger δ values than the ones measured in single filaments. This is even more pronounced in ventral SF parts close to FAs (ROI 2 in Figs. 2e,f) or in dorsal SFs (ROI 3 in Figs. 2e,f); larger δ values appear as progressively redder sticks in the δ images. In these regions, ρ angles also distribute over a large range of orientations, not necessarily along the SF (see zooms in Fig. 2g, compare ROI 6 with ROI 5) and δ angle distributions shift to high values (see polar histogram insets in Figs. 2f and histograms in Fig. 2h, compare ROIs 2-3 with ROI 1). This trend was observed for multiple SFs in all measured cells (see other examples in Supplementary figure S4). At last, in seemingly homogeneous meshworks, AF488 orientations ρ seem to follow preferential directions with much larger distributions (ROI 4 in Figs. 2e,f,h).

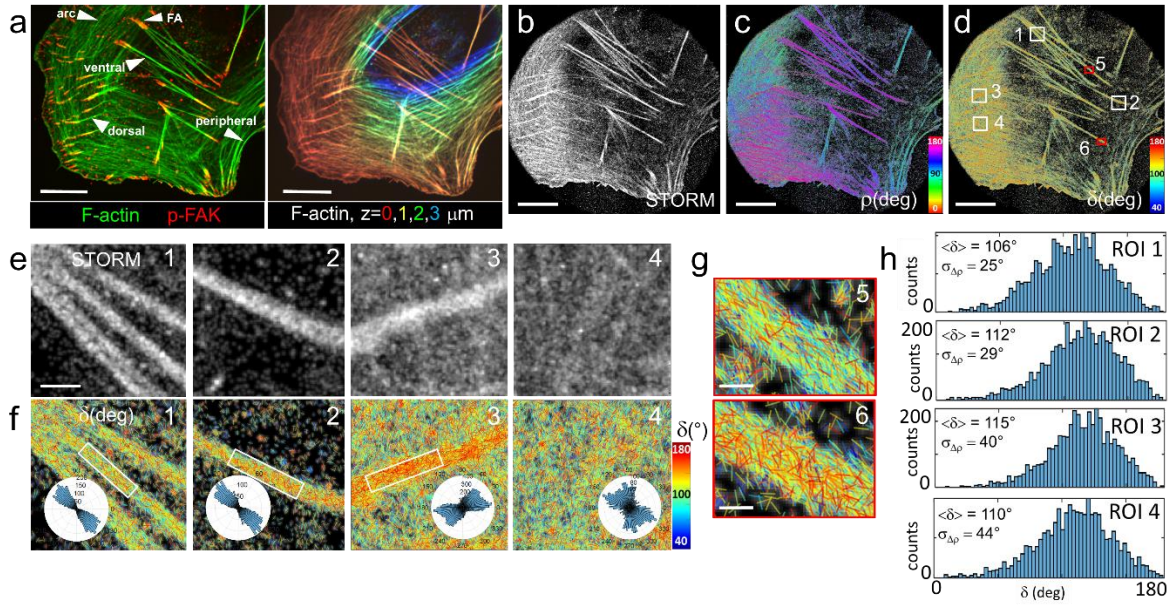

Figure 2. 4polar-STORM imaging of actin filament organization in fixed U2OS cells. (a) Left: Spinning-disk fluorescence image of a U2OS cell (green, AF488-phalloidin-labelled F-actin; red, p-FAK). White arrows indicate focal adhesions (FAs) and the types of stress fibers (SFs) of interest. Right: z-stack mage of F-actin, z is color-coded as indicated. (b) Large field of view single molecule (AF488) localization STORM image of the same cell. (c) Corresponding 4polar-STORM ρ stick image with color-coded orientation measurements. (d) Corresponding 4polar-STORM δ stick image with color-coded wobbling angle measurements. (e) STORM and (f) corresponding δ stick images of zoomed regions of interest (ROI) (see squares in (d)). ROI 1, ventral SF; ROI 2, FA; ROI 3, dorsal SF; ROI 4, meshwork. Insets in (f) depict the polar-plot histograms of ρ in the rectangle region indicated (whole region for ROI 4). (g) δ stick images of zoomed ROIs 5 and 6 (see red squares in (d)) exhibiting respectively low δ and high δ populations. ROI 5, ventral SF; ROI 6, FA. (h) Histograms of δ values for ROIs 1-4. Values of $\langle\delta\rangle$ (over all measured molecules) and of the standard deviation $\sigma_{\Delta\rho}$ of $\Delta\rho = \rho - \langle\rho\rangle$ are shown. For all images, intensities are thresholded above 5×10^4 camera counts and localization precisions are thresholded below 0.15 pixels (σ_{loc} < 20 nm). Scale bars (a-d), 7 μm; (e), 800 nm; (g), 260 nm.

To understand the presence of large δ values and wide ρ distributions in SFs, we investigated possible correlations between these two parameters. We found first that in all observed SFs, large δ values generally correlate with a wide distribution of ρ values (Fig. 3a). This behaviour could physically correspond to molecules that are freely, isotropically rotating, but we exclude such an effect. First, no free phalloidin-fluorophore conjugates are expected given the high affinity of phalloidin for actin filaments. Second, higher wobbling angles were not present in single actin filaments and thin actin bundles. We exclude also a sensitivity of wobbling to actin filament packing within bundles, considering the small size of phalloidin-AF488; single actin filaments do not present packing-related constraints and did not exhibit high wobbling angles. Our hypothesis for the observed high δ values is the presence of 3D oriented actin filaments (off-plane η angle in Fig. 1a) that lead to an overestimation of δ. The use of a relatively low detection NA of 1.2 minimizes the bias induced by 3D orientations as compared to higher NA conditions, but does not entirely exclude this effect. Typically, wobbling molecules with δ_{3D} = 90° oriented off-plane by η = 45° lead to a measured δ = 150° (Supplementary Fig. S1). 3D oriented filaments also naturally lead to larger deviations of ρ. Typically a ρ distribution of $\sigma_{\Delta\rho} = 20°$ for an in-plane filament would increase dramatically to an apparent $\sigma_{\Delta\rho} \sim 90°$ when this filament is tilted off-plane by 45° (Supplementary Fig. S5). To test the hypothesis of possible 3D oriented filaments, we investigated the correlation of δ and ρ with the single molecule detection parameters, in particular their intensity, which is expected to decrease when fluorophores are tilted off plane due to their lower photo-excitation, and the PSF radius, which is expected to increase when molecules are either tilted or out of focus. Large δ values and wider distributions of ρ values are indeed found to correlate with large PSF radii and with the lowest levels of intensities (Fig. 3b,c). Thresholding intensities and σ_{loc} values as above, as well as keeping PSF radii below 1.15 pixels (~150 nm) leads to a net reduction of the populations of high δ values (Fig. 3d; compare with Fig. 2f) (see also Supplementary Fig. S4). Larger populations of large PSF radii can also be found in SFs that are visibly enriched in high δ values (Supplementary Fig. S6). These populations are attributed to molecules tilted off plane (also possibly positioned at slightly different heights), and therefore to populations of filaments that are tilted with respect to the sample plane. Such tilted filaments are found, as expected, more frequently at the FA sites and in dorsal SFs, both of which are expected to contain off-plane filament populations, in contrast to ventral SFs, which lie in the plane of the substrate (Fig. 2a).

Estimation of the off-plane angle can be done qualitatively from the theoretical δ vs η bias dependence (Supplementary Fig. S1). In the case of actin filaments labelled with AF488-phalloidin, we expect $\delta \sim 90°$ for molecules lying in-plane (Fig 1). This value would increase to about $\delta \sim 110°$ for η = 70° and $\delta \sim 150°$ at η = 45° (Supplementary Fig. S1). The population with $\delta > 120°$ ($\eta < 60°$) observed in Fig. 3a is thus attributed to filaments tilted by more than 30° from the sample plane. Thus, selecting only delta values with $\delta < 110°$ ($\eta > 70°$, i.e. within 20° from the sample plane) allows to measure actin filament organization in SFs without a strong bias on $\sigma_{\Delta\rho}$ (Supplementary Fig. S5). Using this criterion, the parameter $\sigma_{\Delta\rho}$ can therefore be used as a minimally-biased quantitative estimate of in-plane actin filament organization in selected regions. $\sigma_{\Delta\rho}$ is seen to decrease in SFs for $\delta < 110°$ (Fig. 3e-f, ROIs 1 and 2, compare with Fig. 2f,h), reaching the $\sigma_{\Delta\rho}$ values in single actin filaments (Fig. 1 g), thus showing now highly aligned actin filaments in ventral SFs and FAs. Regions in dorsal SFs and meshworks depict

now more clearly populations of actin filaments crossing each other, as expected (Fig. 3e-f, ROIs 3 and 4, compare with Fig. 2f) (see also Supplementary Fig. S7). Importantly, the estimated $\sigma_{\Delta\rho}$ is found to be of similar values independently of the radius size thresholding (data not shown), as long as in-plane filaments are selected ($\delta < 110°$).

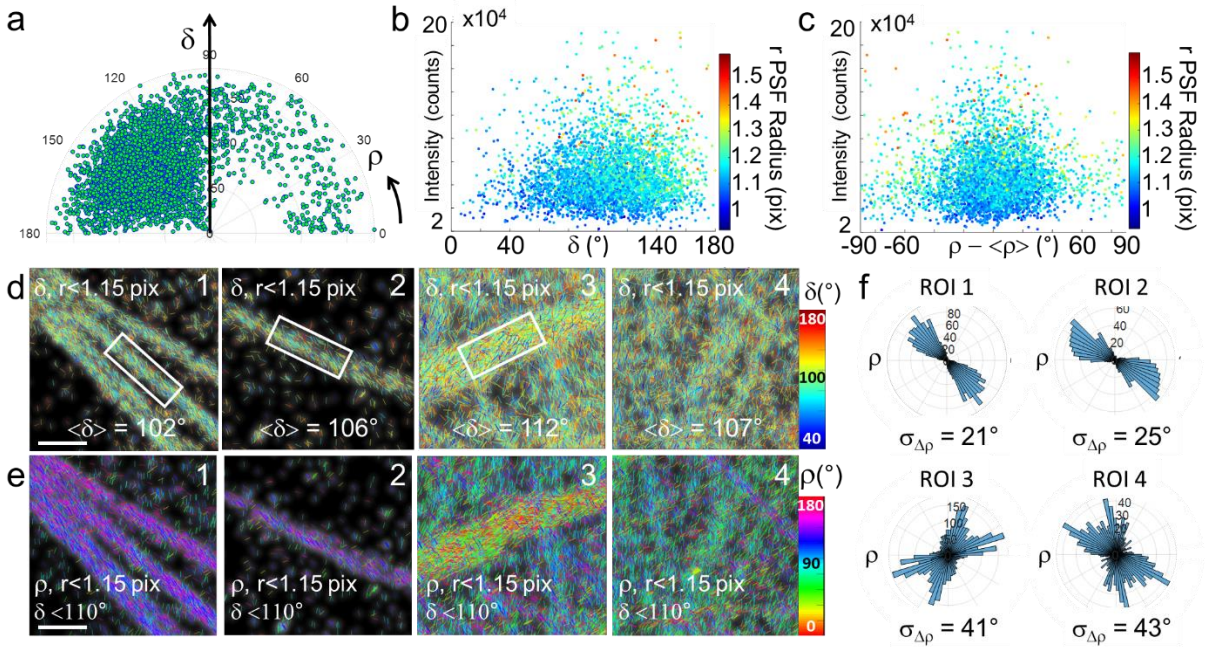

Figure 3. Influence of the detection parameters on 4polar-STORM imaging. (a) Scatter polar representation of (δ,ρ) values obtained in single AF488 molecules (all detected intensities) present in ROI 1 (rectangle in (d)). Each marker is a molecule present in the ROI, plotted using cylindrical coordinates δ as a radius and ρ as an angle respective to the horizontal axis. (b) Same δ values as in (a), using intensity counts as a vertical coordinate, and the PSF radius r as a color code for the markers. Each marker is a single molecule. (c) Same representation using, for the horizontal axis, ρ values centered with respect to their average orientation <ρ>. (d) Same 4polar-STORM images as in Fig. 2e,f, depicting δ sticks only for molecules for which r < 1.15 pixels (149 nm). The corresponding average <δ> over all measured molecules (present in the rectangle for ROIs 1-3 or the whole region for ROI 4) are shown. (e) Same ROIs as in (d) showing ρ stick images only for molecules with $\delta < 110°$. (f) Corresponding polar-plot histograms of ρ for regions indicated in (e). The corresponding $\sigma_{\Delta\rho}$ values are shown. Scale bar (d-e), 800 nm.

Our analysis emphasizes two novel possibilities that the 4polar-STORM method offers for the investigation of actin filament organization. First, the wobbling of single fluorophores can be used for the quantification of their off-plane tilt orientations, exploiting the degree of bias even at a slightly reduced detection NA. Second, the lowest wobbling values obtained in a population of fluorophores can be used to select in-plane populations of actin filaments and study their organization in a quantitative manner. Not quantifying these sources of bias can lead to errors of interpretation in the measured organizations, especially at the high detection NAs generally used[22,23,24]. In what follows, we

exploit these considerations to quantitatively compare actin filament organization in different structures of the cell.

Actin filament organization imaging by 4polar-STORM in-plane selection

We first analysed actin filament organization in different types of SFs in cultured U2OS cells on unpatterned or micropatterned coverslips (see Methods), quantifying $\sigma_{\Delta\rho}$ for molecules with $\delta < 110°$. In what follows, the PSF radius of single molecules is not thresholded, results being very similar in both conditions. Regions defining ventral, peripheral, dorsal SFs as well as transverse arcs and FAs are measured by 4polar-STORM. We combine phalloidin stainings with immunostainings for a FA protein, the phosphorylated form of focal adhesion kinase, p-FAK, in order to define the different types of SFs based on their association with FAs[42,43] (Fig. 2a). A z-stack of the cell further allows us to visualize off-plane tilted structures (Fig. 2a). While ventral, peripheral and arc SFs are lying in the sample plane, dorsal SFs are the most tilted ones. $\sigma_{\Delta\rho}$ values were measured in rectangular ROIs of typically (0.5-1 μm) x 100 nm in size. $\sigma_{\Delta\rho}$ exhibits very large distributions, due to variations in actin filament organization among SFs within a given cell and across cells (Fig. 4a). Among the measured SFs, ventral SFs exhibit the highest filament alignment (lowest $\sigma_{\Delta\rho}$ value), with the average $\sigma_{\Delta\rho}$ close to that measured in single filaments ($<\sigma_{\Delta\rho}> \sim 25°$). $\sigma_{\Delta\rho}$ values for transverse arc SFs are slightly higher, suggesting the presence of less well-aligned actin filaments or/and filaments crossing each other. Such organization is fully consistent with the proposed mechanisms of transverse arc assembly, involving both the progressive fusion and alignment of actin filament fragments and myosin filament stacks, and connections of forming arcs with dorsal SFs[44,45,46]. $\sigma_{\Delta\rho}$ values for peripheral SFs are, surprisingly, even larger, suggesting that peripheral SFs contain a larger population of actin filaments in various directions. This observation correlated with the fact that the measured peripheral SFs were often thicker than the measured ventral ones, which suggests that thicker SFs contain more various actin filaments directions. This hypothesis is in line with observations of actin bundles fusing with or splitting from peripheral fibers and with recent work showing that peripheral SFs and the cortical meshwork form a continuous contractile network [47]. FAs, regardless their association with ventral or dorsal SFs, depict a much wider distribution of $\sigma_{\Delta\rho}$ values, containing both highly aligned actin filaments and actin filaments in mixed orientations. We hypothesize that this organization reflects the dynamical nature of FAs, whose precise assembly and maturation depend on the local mechanical environment[48,49]. At last, dorsal SFs exhibit the highest $\sigma_{\Delta\rho}$ values with $<\sigma_{\Delta\rho}> \sim 35°$. We attribute these high values to the very nature of dorsal SF assembly involving extensive interconnections along their length with transverse arc SFs[42,43]. Depicting all $<\delta>$ values measured in all ROIs confirms that peripheral SFs, FAs and dorsal SFs contain the largest population of filaments tilted off plane, with the lowest proportion of single molecules with $\delta < 110°$ (Fig. 4a).

These results show that while peripheral SFs are known to be under a larger mechanical strain than central ventral SFs[50], their higher mechanical tension is not necessarily accompanied with a higher alignment of actin filaments in-plane. To probe the sensitivity of actin filament organization in SFs to contractility, we treated U2OS cells with blebbistatin, a drug that inhibits myosin II activity and therefore acto-myosin bundle contractility. To minimize dispersions due to SF heterogeneities, we performed this experiment on cells adhering to H-shaped micropatterned substrates of a well-defined

size, concentrating on peripheral SFs (see Methods). Blebbistatin treatment leads eventually to the dissociation of the contractile peripheral SFs[51] (also seen in our data). Blebbistatin concentration and incubation time were thus kept low enough to induce a loss in contractility, evidenced by the concave shape of relaxed SFs, while preserving the apparent macroscopic integrity of the SFs (Fig. 4b). The single molecule localization image alone (STORM, Fig. 4b) cannot inform us on the underlying actin filament organization in the relaxed SFs. 4polar-STORM measurements, however, show a slight decrease of actin filament alignment, with a statistically significant increase of $<\sigma_{\Delta\rho}>$ from 26° to 32° (Fig. 4c), and also an enrichment of 3D oriented filaments as seen from the increase of $<\delta>$ (Fig. 4d). Contractility loss induced by myosin II inactivation is therefore correlated to a decrease of actin filament organization which is also visible from the 4polar-STORM ρ images (Fig. 4b). Representative distributions of single-molecule orientations ρ in control and blebbistatin-treated SFs are shown in Fig. 4b and quantified in Fig. 4e, for both in-plane ($\delta < 110°$) and off-plane ($\delta > 120°$) filament populations. The spreading of the distributions induced by blebbistatin confirms a decrease in actin filament alignment and a concomitant increase in 3D oriented filament populations as schematically represented in Fig. 4f. 4polar-STORM measurements thus reveal that actin filament organization in SFs is sensitive to acto-myosin contractility, with myosin II inhibition inducing a loss in actin filament alignment at the nanometer-scale.

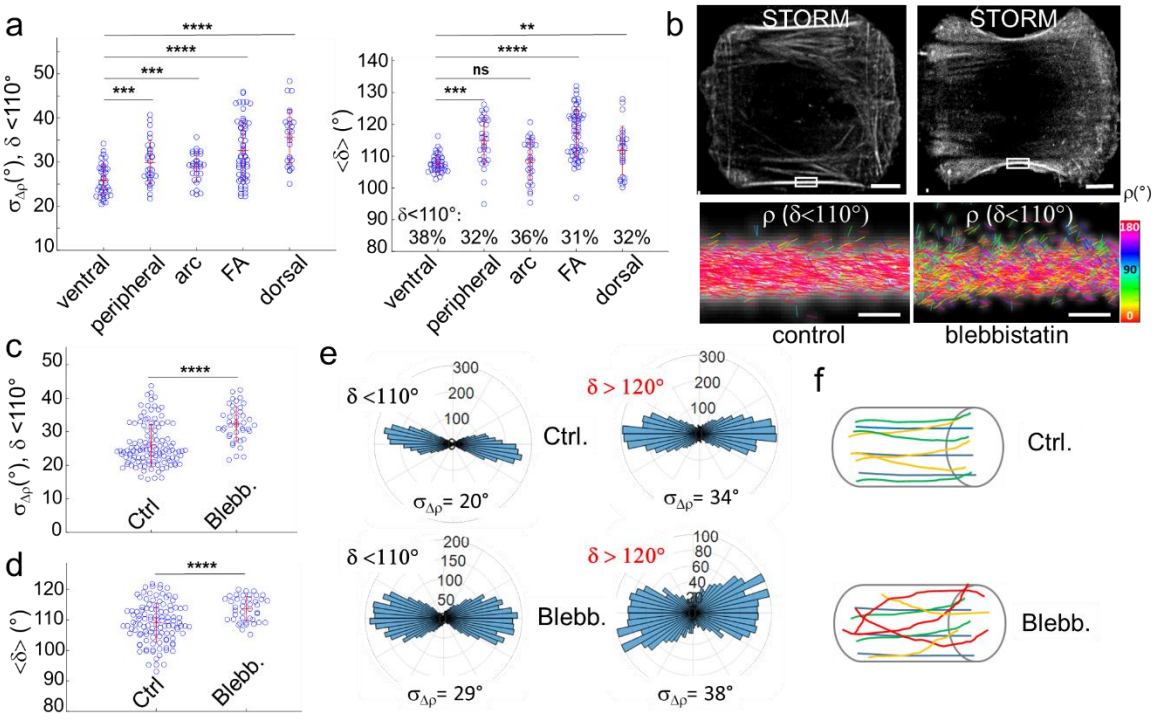

Figure 4. 4polar-STORM imaging of actin filament organization in different types of stress fibers. (a) Left: $\sigma_{\Delta\rho}$ (standard deviation of $\Delta\rho = \rho - <\rho>$) values measured in ROIs on different types of SFs, using only molecules with $\delta < 110°$. The numbers of measured ROIs are as follows: n=42 (ventral), 32 (peripheral), 30 (arc), 51 (FA), 28 (dorsal) from a total of 8 cells. Typically, a few thousands of molecules per ROI are measured. Right: same analysis, plotting $<\delta>$ (average of δ measured for each ROI, all δ values selected). For each SF type, the percentage of the δ population with $\delta < 110°$ is indicated. Statistical significance of scatter plots: ns (p>0.05); ** (p < 0.01); *** (p < 0.001); **** (p < 0.0001) (T-test). All comparisons are made with respect to the ventral SF population.

(b) top: STORM images of control and blebbistatin-treated U2OS cells on micropatterns. Scale bars, 6.5 μm; bottom: 4polar-STORM ρ stick images of zoomed regions (rectangles in the STORM images). Scale bars, 500 nm. (c) Effect of blebbistatin on peripheral SFs (see Methods for blebbistatin treatment). $\sigma_{\Delta\rho}$ values reported for all ROIs, using only molecules with $\delta < 110°$. 4 cells were analysed per condition, using in total 87 ROIs in control cells and 43 ROIs in treated cells. (d) $<\delta>$ values reported for all ROIs (all δ selected). (e) Polar-plot histograms of ρ in the zooms shown in (b), for $\delta < 110°$ (left) and $\delta > 120°$ (right). The corresponding $\sigma_{\Delta\rho}$ values are shown. (f) Schematic representations of the SFs observed in control and blebbistatin-treated conditions, showing highly-aligned actin filaments in 2D (top) and disorganized filaments in 3D (bottom).

At last, we investigated actin filament organization in dense networks at the leading edge of B16 melanoma cells (Fig. 5a). We concentrate in particular on the lamellipodium, which spans a few micrometers at the cell border[36]. Again, the single molecule localization images alone (STORM in Fig. 5a,d) do not provide any information on how single AF488-phalloidin molecules orient with respect to one another and thus on the nanometer-scale organization of the labelled actin filaments; the very high filament density in these networks makes it even more challenging to decipher the precise arrangement of filaments. Remarkably, the contour of the cells imaged by 4polar-STORM shows different (ρ,δ) distributions than in the rest of the cell (Fig. 5b,c). Within the first hundreds of nanometers from the cell contour, single molecules exhibit wide distributions of orientations (ρ) and high wobbling (δ) values, signatures of more disorganized, off-plane actin filament populations. Selecting only in-plane filaments ($\delta < 110°$) shows that actin filaments in these dense networks are not oriented isotropically, but that there are visible preferred orientations which cannot be detected in the single molecule localization images alone[25] (Fig. 5d and quantification in Fig. 5e). Single molecule orientation distributions at the cell border (ROIs 1,2,4-8 in Fig. 5b) reveal in general the presence of two main populations with different contributions (Fig. 5e). Generally, one of the two orientation populations appears to predominate (ROIs 1,6-8). However, in some regions (ROIs 5), the two populations tend to contribute equally into a bimodal distribution, which becomes more isotropic when off-plane molecules are considered ($\delta > 120°$). This behaviour has been observed in all cells measured (see another example in Supplementary Fig. S8). We note that these distributions are very different from those found in SFs, which exhibit much narrower distributions with a preferred orientation, even when considering off-plane molecules (ROI 10). At last, narrow distributions are found in microspikes (ROIs 3,9), which is a signature of parallel actin bundles within the lamellipodium, despite their close proximity to bimodal distributions (see ROIs 2 and 4 which surround ROI 3).

Remarkably, the angle between the two peaks of the observed bimodal distributions is close to 70°, with some variations along the cell contour, and points towards the normal to the membrane contour (Fig. 5e). This is reminiscent of observations made by EM where actin filaments display a bimodal angular distribution, with filament orientations peaking at 35° and -35° with respect to the direction of membrane protrusion[34,35,36]. This so-called dendritic organization was attributed to the angle imposed by the Arp2/3 complex involved in actin filament branching in those regions[36,52]. Bimodal orientation distributions in 4polar-STORM images were present in ROIs from hundreds of nanometers to micrometers sizes, and were variable depending on the region of the cell contour, emphasizing the importance of large field of view observations.

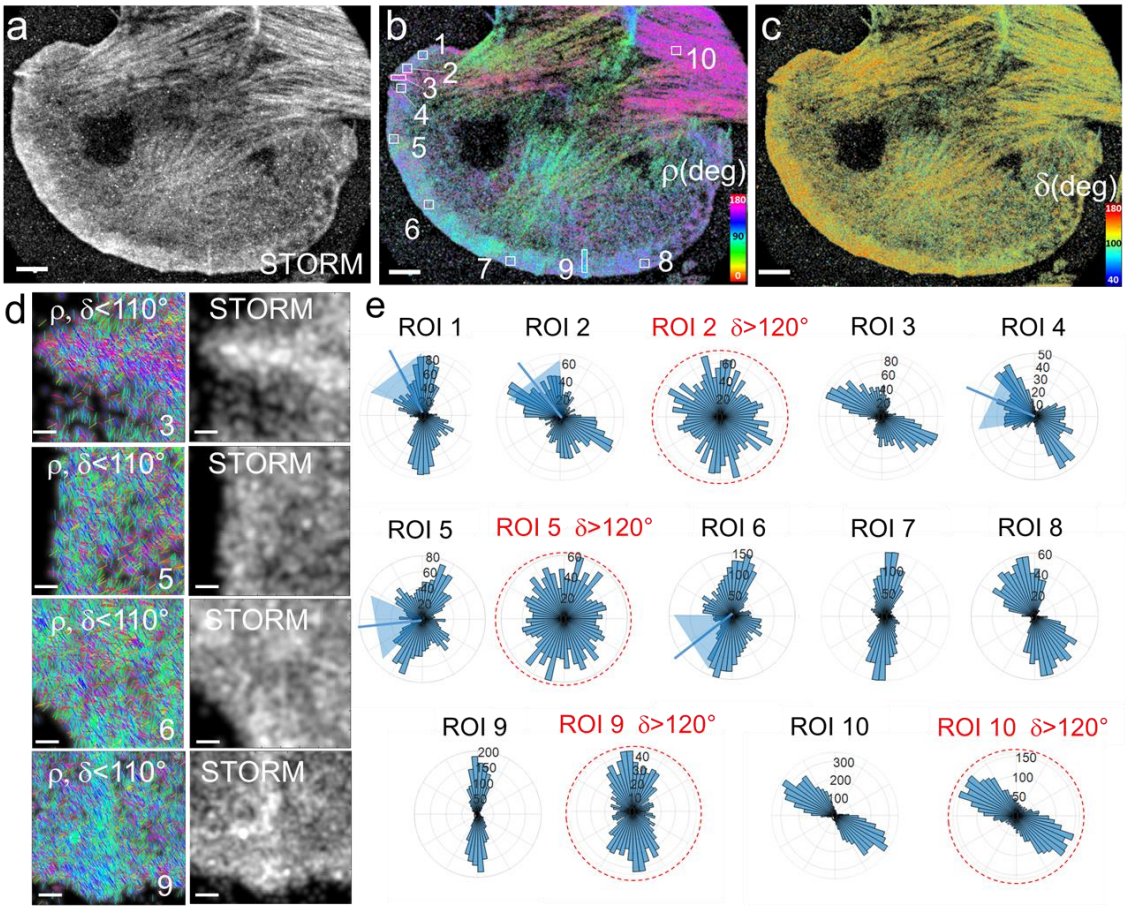

Figure 5. 4polar-STORM imaging of actin filament organization in lamellipodia. (a) Single molecule localization STORM image of a B16 cell labelled with AF488-phalloidin. (b) Corresponding 4polar-STORM ρ stick image with color-coded orientation measurements. (c) 4polar-STORM δ stick image with color-coded wobbling angle measurements. (d) Examples of ρ stick images showing molecules with δ < 110° and corresponding STORM images in selected ROIs (squares in (b)). ROIs 1-9, regions in the lamellipodium; ROI 3,9, microspikes; ROI 10, SF. (e) Polar-plot histograms of ρ for the regions shown in (b). The condition δ < 110° is used, except for red-circled histograms for which δ > 120° molecules are selected. Scale bars (a-c), 4 μm; (d), 260 nm.

The variations in the precise distribution of actin filament orientations at the cell edge, and the non-negligible presence of 3D orientations, are consistent with recent findings in the literature based on EM and modelling[4]. A range of angular distributions of actin filament orientations has been evidenced, which appears to be more complex and heterogeneous than a pure bimodal distribution with peaks positioned at the 70° branching angle[53]. This angular spread depends on the cell mechanical load[54], and the precise geometry of filament assemblies, not necessarily pointing towards the membrane normal, depends on the modulation of the protrusion rate[55,56]. Additionally, actin filament organization within the lamellipodium sheet is known to extend in 3D, with possibly different organizations at the cell surface and in the upper layer as evidenced recently in studies using 3D super-resolution localization microscopy[25] or cryo-tomography EM[57]. The 4polar-STORM results, which do not differentiate between specific actin layers, suggest the co-existence of both preferred angular distributions of actin filament orientations and populations of 3D oriented filaments.

Discussion

We developed a new super-resolution fluorescence microscopy method, called 4polar-STORM, which allows simultaneous measurements of single molecule localization and orientation in 2D, as well as an indirect evaluation of their 3D orientation. The 4polar-STORM analysis permits to evaluate quantitatively both the orientation and wobbling angles of single molecules, thus enabling the accurate determination of their organization. A detailed theoretical analysis of the dependence of the orientation and wobbling parameters on different sources of bias, either originating from SNR conditions or physical features, such as 3D molecular orientations or a high detection NA, is used to define appropriate detection conditions and analysis procedures for the minimally biased determination of molecular organization at the nanometer scale. It is important to note that the majority of polarized single molecule experiments have been performed under high NA conditions so far. This prevents the physical interpretation of wobbling values and thus an unbiased determination of the underlying molecular organization[23,24]. Other alternatives such as PSF engineering necessitate more complex signal processing to achieve quantitative measurements, and can be challenged in high density-labelled samples[14,19].

To highlight the potential of 4polar-STORM to measure molecular organization in complex protein assemblies, we measured the nanometer-scale organization of actin filament-based structures involved in the adhesion and motility of mammalian cells. We focused on different types of stress fibers made of actin filament bundles and on the actin filament meshwork of the lamellipodium. We exploited the sensitivity of orientation and wobbling parameters to molecules lying off-plane to evidence the non-negligible contribution of 3D orientations in the measured populations of actin filaments, both in SF bundles and in the flat lamellipodium. Selecting the lowest wobbling values from measured single molecules permits to select only in-plane filament populations and determine their organization in a quantitative manner. This analysis permitted to evidence the very high actin filament alignment in all types of SFs, in line with EM studies[31,32], but to also reveal differences in their nanometer-scale organization, consistently with their different modes of assembly and function in the cell. Thin 2D ventral and transverse arc SFs are made of highly aligned actin filaments, while thick peripheral SFs, off-plane oriented dorsal SFs, and FAs containing filament populations of mixed orientations, were seen to contain a non-negligible population of filaments with 3D off-plane orientations. Low doses of blebbistatin that inhibited myosin II activity in contractile peripheral SFs, while preserving their macroscopic integrity, resulted in a perturbation of the nanometer-scale organization of actin filaments, emphasizing the key role of myosin II in the organization of actin filaments in contractile SFs. Importantly, in-plane measurements of actin filament organization permitted us to investigate the organization of dense assemblies that is not accessible by single molecule localization imaging alone, in particular in the lamellipodium at the leading edge of motile cells. 4polar-STORM imaging revealed that the actin filaments in the lamellipodial meshwork are not oriented randomly but that they organize in preferred angular distributions, including bimodal distributions previously observed by electron microscopy. It is important to note that these characteristic features of the dendritic organization of the lamellipodium have not been observed with other super-resolution light microscopy methods.

These results show altogether the added value of combining localization and orientation measurements, and highlight the potential of 4polar-STORM to investigate the nanometer-scale organization of actin filaments in complex arrangements which are hardly accessible in standard optical super-resolution microscopy. In particular, the complex geometries of actin filaments close to the cell membrane and their link with local contractile and protrusive activity are poorly understood. Additionally, little is known on the organization of actin filaments in cell adhesion-mediating structures which play a large role in cell mechanics, in particular focal adhesions. Assessing the nanometric organization of actin filaments, and the contribution of 2D vs 3D oriented populations of filaments, at various stages of FA formation and maturation promises to permit us to understand how such complex molecular machineries assemble in order to sense, respond and adapt to mechanical stimuli. We note that while AF488-phalloidin is used in the present study, our method is fully compatible with a wide variety of labels as long as the orientational flexibility of the fluorophore is not very high. In particular, actin labelling by Atto633-phalloidin[10] or silicon rhodamine-jasplakinolide (SiR-actin)[24,58], have been reported to exhibit low wobbling. Genetically encoded probes for actin filament orientation studies are also currently being developed[59], using strategies which could be extended to other proteins of interest. Such approaches which are amenable to live-cell measurements promise to open new directions for orientational dynamics studies, combining for instance single molecule orientation measurements with single particle tracking PALM[60]. Wobbling measurements in the case of fluorescent proteins, whose size is typically comparable to the size of the labelled protein of interest, might also reveal packing-related constraints and could thus provide additional protein organization readouts. Although the present work focuses on the implementation of 4polar-STORM for deciphering the organization of actin filaments, the framework we built regarding theoretical considerations for the retrieval of orientation parameters and the definition of appropriate acquisition and analysis procedures, can be easily adapted for the study of any molecule. The methodology of 4polar-STORM is also compatible with two-color localization and orientation measurements and thus can provide insights into the functional interplay between the nanometric organizations of interacting partners; the link between conformational changes in activated integrins and actin filament remodeling is such an example. At last, 4polar-STORM is compatible with 3D localization schemes, including astigmatism[61] or multiplane[62,63] strategies, and can therefore be adapted for exploring the full 3D organization of a large variety of biological structures[64].

Materials and Methods

4polar-STORM optical setup. Measurements are carried-out on a custom epi/TIRF-fluorescence microscope, whose detection path is adapted to retrieve four polarization states of the single molecule fluorescence images. The excitation light source is a continuous laser emitting at 488 nm (Sapphire 488LP-200, Coherent), whose beam is expanded by a telescope and circularly polarized by a quarter waveplate (AQWP10M-580, Thorlabs). A set of mirrors reflect the beam towards the microscope, followed by a large focal length lens (f = 400 mm) to focus the beam in the back focal plane of the objective, to provide an illumination field of view with a diameter of about 100 µm. After the reflection on a dichroic mirror (DI02-R488, Semrock Rochester NY), the excitation light is focused onto the sample by an oil immersion objective lens (Plan Apo 100×, NA = 1.45, Nikon). The emitted fluorescence is collected back by the same objective lens, passes through the dichroic mirror and a band pass emission

filter (FF01-525/40, Semrock Rochester NY). At the microscope exit a non-polarizing beam splitter separates the beam in two paths, each of them being built up with a 1x relay imaging telescope that uses two (f 150 mm) lenses. In the first path, a Wollaston prism (separation angle 5°, CVI Laser Optics) is placed at the back focal intermediate image plane, aligned for 0°-90° polarization split. In the second path, a similar Wollaston prism is placed just after an achromatic half wave plate (AHWP05M-600, Thorlabs), to provide 45°-135° polarized images. The two beams are recombined by a mirror reflection of the first path, and refocused on the EMCCD camera detection plane (iXon Ultra 888, Andor, 13 μm pixel size), such as to fill the CCD chip with four polarized images. The size of the images is set by a diaphragm placed in the first image plane at the exit of the microscope (typical image field of view, 40 μm x 40 μm). In addition, two diaphragms are placed in intermediate planes conjugated to the back focal plane of the objective in order to reduce the detection numerical aperture to NA_{det} = 1.2. The imaging lens provides a total magnification of ×100, corresponding to a pixel size of 130 nm on the EMCCD. The stability of the focus throughout the measurement is ensured by a commercial system (Perfect Focus System, Nikon). For initial positionning, the sample is mounted on a XYZ piezo stage (Physik Instrumente). The acquisition parameters are controlled by a commercial imaging software (AndorSolis, Andor). For STORM imaging, a first fluorescence image is recorded with low intensity (~ 500 W/cm^2, below STORM blinking conditions), ensuring the identification of relevant parts of the sample. The intensity is then raised to 5-8 kW/cm^2, which is a typical level to provide a good compromise between signal level and blinking rate. The images are acquired at a rate of 100 ms/image, camera gain 300, with a total of about 30,000 images depending on the molecular density.

Cell culture. 4polar-STORM measurements were made in U2OS osteosarcoma cells (Fig. 1-4) and B16-F1 mouse melanoma cells (Fig.5). Naive U2OS cells (gift from Flavio Maina, IBDM, France) were used for assessing the effect of blebbistatin. U2OS CA-MLCK cells (gift from Sanjay Kumar, UC Berkeley, USA) cultured in 0 ng/mL doxycycline were used for all other experiments. U2OS cells were maintained in McCoy's 5A medium (ThermoFisher Scientific, 26600-080) supplemented with 10% fetal bovine serum (Biowest, S181H), 100 U/mL penicillin and 100 μg/mL streptomycin (Sigma, P4333) in a humidified incubator at 37°C and 5% CO2. B16-F1 cells (gift from Klemens Rottner, Technische Universität Braunschweig, Germany) were cultured in DMEM (ThermoFisher Scientific, 41966-029) supplemented with 10% fetal bovine serum (PAA Laboratories, A15-102), 100 U/mL penicillin and 100 μg/mL streptomycin (Sigma, P4333) in a humidified incubator at 37°C and 5% CO2.

Cell preparation for 4polar-STORM. U2OS cells. 24 mm-diameter high-precision (170 μm ± 5 μm) glass coverslips (Marienfeld, 0117640) were cleaned with base piranha (Milli-Q water, 30% ammonium hydroxide, 35% hydrogen peroxide at a 5:1:1 volume ratio) for 15 min, rinsed with Milli-Q water for 2 x 5 min in a bath sonicator, sonicated in 70% ethanol for 5 min, and air-dried before coating with fibronectin (SIGMA F1141) for 2 h at room temperature (RT) and at a final fibronectin concentration of 20 μg/mL in PBS. For experiments with micropatterned substrates, medium-size (1100 μm^2) H-shaped patterns from CYTOO (10-900-00-18) were similarly coated with 20 μg/mL fibronectin. U2OS cells were seeded onto fibronectin-coated coverslips and allowed to spread for 5 h on micropatterned substrates or overnight on nonpatterned ones. Cells were fixed for 15 min with 4% formaldehyde (Electron Microscopy Sciences 15714) in cytoskeleton buffer (10 mM MES pH 6.1, 150 mM NaCl, 5 mM EGTA, 5 mM $MgCl_2$, 5 mM glucose), washed for 2 x 5 min in PBS, then permeabilized and blocked in

phosphate-buffered saline (PBS) containing 0.1% saponin and 10% bovine serum albumin (BSA) for 1 h at RT. Cells were incubated successively with primary rabbit anti-phospho-FAK antibodies at 1:200 (ThermoFisher Scientific 44-624G) and secondary donkey anti-rabbit Alexa Fluor 647-conjugated IgG secondary antibodies at 1:1000 (ThermoFisher Scientific A-31573) each for 1 h at RT and with three 10-min washes in-between antibody incubations. After five 6-min washes, cells were incubated with 0.5 μM Alexa Fluor 488 (AF488)-phalloidin (ThermoFisher Scientific A12379) in 0.1% saponin/10% BSA/PBS overnight at 4°C in a humidified chamber. For 4polar-STORM measurements, coverslips with stained cells were mounted in an Attofluor cell chamber (ThermoFisher Scientific A7816) with freshly prepared STORM imaging buffer (see composition below) and the chamber covered with a glass coverslip to minimize contact with oxygen. To visualize focal adhesions in order to define the types of stress fibres measured, AF488-phalloidin and phospho-FAK-co-stained cells were imaged before each STORM acquisition on an optical setup employing a confocal spinning disk unit (CSU-X1-M1 from Yokogawa) connected to the side-port of an inverted microscope (Eclipse Ti-U from Nikon Instruments), using a Nikon Plan Apo ×100/1.45 NA oil immersion objective lens, 488- and 641-nm laser lines (Coherent) and an iXon Ultra 888 EMCCD camera (1024×1024 pixels, 13×13 μm pixel size, Andor, Oxford Instruments). z-stacks were acquired with a Δz interval of 0.5 μm.

B16-F1 cells. 24 mm-diameter high-precision (170 μm ± 5 μm) glass coverslips (Marienfeld, 0117640) were sonicated in 70% ethanol for 5 min and air-dried before coating with mouse laminin (SIGMA L2020) for 1 h at RT and at a final laminin concentration of 25 μg/mL in coating buffer (50 mM Tris-HCl pH 8, 150 mM NaCl). B16-F1 cells were seeded onto laminin-coated coverslips and allowed to spread overnight. To stimulate lamellipodia formation, cells were treated with aluminum fluoride for 15 min by adding $AlCl_3$ and NaF to final concentrations of 50 μM and 30 mM, respectively, in pre-warmed, full growth medium. Cells were fixed for 20 min with a mixture of prewarmed (37°C) 0.25% glutaraldehyde (Electron Microscopy Sciences 16220) and 4% formaldehyde (Electron Microscopy Sciences 15714) in cytoskeleton buffer, and treated with fresh sodium borohydride (1 mg/mL) in PBS for 2 x 5 min to reduce background fluorescence. Cells were washed in PBS for 3 x 5 min before an overnight incubation with 0.5 μM AF488-phalloidin in 0.1% saponin/10% BSA/PBS at 4°C in a humidified chamber. For 4polar-STORM measurements, coverslips were mounted as for U2OS cells.

Blebbistatin treatment. Blebbistatin from Sigma (B0560) was prepared at 10 mM in DMSO. U2OS cells were seeded onto fibronectin-coated medium-size H-shaped patterns from CYTOO and allowed to spread for 5 h, as detailed above. Cells were incubated for 15 min with 50 μM blebbistatin (i.e. in medium also containing 0.5% DMSO due to the blebbistatin stock dilution), or with medium containing 0.5% DMSO (control cells). Cells were fixed with 4% formaldehyde in cytoskeleton buffer for 15 min, and washed in PBS for 2 x 5 min before an overnight incubation with 0.5 μM AF488-phalloidin in 0.1% saponin/10% BSA/PBS at 4°C in a humidified chamber. Cells were mounted for 4polar-STORM measurements as detailed above.

Reconstitution of single actin filaments for 4polar-STORM. Lyophilized rabbit skeletal muscle G-actin (Cytoskeleton, Inc. AKL99) was resuspended to 5 mg/mL (119 μM) in G-buffer (5 mM Tris-HCl pH 8, 0.2 mM Na_2ATP, 0.1 mM $CaCl_2$, 1 mM DTT), aliquots snap-frozen in liquid nitrogen and stored at −80°C. Frozen aliquots were thawed and centrifuged for 30 min at 120,000 g in a benchtop Beckman air-driven ultracentrifuge (Beckman Coulter Airfuge, 340401) to clear the solution from aggregates. Clarified G-

actin was kept at 4°C and used within 3-4 weeks. For reconstitution experiments, G-actin was polymerized at 5 μM final concentration in actin polymerization buffer (5 mM Tris-HCl pH 8, 50 mM KCl, 1 mM $MgCl_2$, 0.2 mM Na_2ATP, 1 mM DTT) in the presence of 5 μM AF488-phalloidin for at least 2 h at RT. Flow cells for measurements on reconstituted actin filaments were prepared as follows. Microscope glass slides and coverslips were cleaned for 15 min in base-piranha solution, rinsed twice, 5 min each, with Milli-Q water in a bath sonicator, and stored in ethanol up to one month. To assemble flow cells, slides and coverslips were dried with synthetic air, and ~10 μL channels were assembled by sandwiching ~2-mm-wide and ~2.5-cm-long strips of Parafilm between a cleaned glass slide and coverslip and melting on a hot plate at 120°C. The chambers were incubated for 45 min with 1 M KOH, rinsed with actin polymerization buffer, incubated for another 15 min with 1 mg/mL poly-L-lysine (PLL; Sigma P8920), and rinsed with actin polymerization buffer. Reconstituted AF488-phalloidin-labelled actin filaments were diluted to 0.1-0.2 μM, loaded into the PLL-coated flow channels and left for 15 min to immobilize actin filaments. Actin polymerization buffer was then exchanged with STORM imaging buffer (see composition below), and flow channels sealed with VALAP (1:1:1 vasoline:lanoline:paraffin). The typical experimental conditions were TIRF illumination, laser power 150 mW, camera gain 300 and 200-ms integration time. A stack of 5000 images was used for 4polar-STORM imaging. The materials and chemicals for glass cleaning were as follows. Glass slides (26x76 mm) from Thermo Scientific (AA00000102E01FST20). Glass coverslips (24x60 mm) from Thermo Scientific (BB02400600A113FST0). Ammonium hydroxide solution from SIGMA (221228). Hydrogen peroxide solution from SIGMA (95299).

STORM imaging buffer preparation. The final composition of the buffer for 4polar-STORM measurements was 100 mM Tris-HCl pH 8, 10% w/v glucose, 5 U/mL pyranose oxidase (POD), 400 U/mL catalase, 50 mM β-mercaptoethylamine (β-MEA), 1 mM ascorbic acid, 1 mM methyl viologen, and 2 mM cyclooctatetraene (COT). D-(+)-glucose was from Fisher Chemical (G/0500/60). POD was from Sigma (P4234-250UN), bovine liver catalase from Calbiochem/Merck Millipore (219001-5MU), β-MEA from Sigma (30070), L-ascorbic acid from Sigma (A7506), methyl viologen from Sigma (856177), and COT from Sigma (138924). Glucose was stored as a 40% w/v solution at 4°C. POD was dissolved in GOD buffer (24 mM PIPES pH 6.8, 4 mM $MgCl_2$, 2 mM EGTA) to yield 400 U/mL, and an equal volume of glycerol was added to yield a final 200 U/mL in 1:1 glycerol:GOD buffer; aliquots were stored at -20°C. Catalase was dissolved in GOD buffer to yield 10 mg/mL, and an equal volume of glycerol was added to yield a final 5 mg/mL (230 U/μL) of catalase in 1:1 glycerol:GOD buffer; aliquots were stored at -20°C. β-MEA was stored as ~77 mg powder aliquots at -20°C; right before use, an aliquot was dissolved with the appropriate amount of 360 mM HCl to yield a 1 M β-MEA solution. Ascorbic acid was always prepared right before use at 100 mM in water. Methyl viologen was stored as a 500 mM solution in water at 4°C. COT was prepared at 200 mM in DMSO and aliquots stored at -20°C. After mixing all components to yield the final buffer composition, the buffer was clarified by centrifugation for 2 min at 16,100 g, and the supernatant kept on ice for 15 min before use. Freshly prepared STORM buffer was typically used within a day.

Supplementary Information

Supplementary Note 1. Model and retrieval of orientation parameters

Acknowledgements

This research has received funding from the « Investissements d'Avenir » French Government program managed by the French National Research Agency ANR (ANR-16-CONV-0001), from Excellence Initiative of Aix-Marseille University A*MIDEX (ANR-11-IDEX-0001), European Union's Horizon 2020 research and innovation programme under the Marie Sklodowska-Curie grant agreement No 713750, and the SEPTIMORF and 3DPolariSR ANR grants (ANR-17-CE13-0014; ANR-20-CE42-0003). This work was also supported by INRIA in the frame of NAVISCOPE-IPL (INRIA Project Lab). The authors are grateful to Arita Silapetere (Humboldt Universitat zu Berlin, Germany) for the assistance in the initiation of the project and Louwrens Van Dellen (Purplecode Aix en Provence, France) for help in the experimental acquisition programming. The authors further acknowledge useful discussions of the results with Klemens Rottner (Technische Universität Braunschweig, Germany).

Author Contributions

S.B and M.M conceived and initiated the project. C.V.R built the optical system, performed experiments on cells and analysed the data with S.B. V.C performed experiments on single actin filaments and analysed the data. C.A.V.C wrote the data processing algorithm. C.V.R and S.B wrote part of the data analysis algorithms. All authors wrote the paper and contributed to the scientific discussion.

Author information

The authors declare that they have no competing financial interests. Correspondence and requests for materials should be addressed to the corresponding author.

Data availability

The datasets generated and analysed during the current study are available from the corresponding author on reasonable request.

Code availability

The code used to process and analyse the data during the current study are available from the corresponding author on reasonable request.

References

1. Winkelman, J. D. *et al.* Fascin- and α-Actinin-Bundled Networks Contain Intrinsic Structural Features that Drive Protein Sorting. *Curr. Biol.* **26**, 2697–2706 (2016).
2. Ennomani, H. *et al.* Architecture and Connectivity Govern Actin Network Contractility. *Curr. Biol.* **26**, 616–626 (2016).
3. Svitkina, T. The actin cytoskeleton and actin-based motility. *Cold Spring Harb. Perspect. Biol.* **10**, (2018).
4. Holz, D. & Vavylonis, D. Building a dendritic actin filament network branch by branch: models of filament orientation pattern and force generation in lamellipodia. *Biophysical Reviews* vol. 10 1577–1585 (2018).
5. Dmitrieff, S. & Nédélec, F. Amplification of actin polymerization forces. *Journal of Cell Biology* vol. 212 763–766 (2016).
6. Hess, S. T., Girirajan, T. P. K. & Mason, M. D. Ultra-high resolution imaging by fluorescence photoactivation localization microscopy. *Biophys. J.* **91**, 4258–4272 (2006).
7. Betzig, E. *et al.* Imaging Intracellular Fluorescent Proteins at Nanometer Resolution. *Science (80-.).* **313**, 1642–1645 (2006).
8. Rust, M. J., Bates, M. & Zhuang, X. Sub-diffraction-limit imaging by stochastic optical reconstruction microscopy (STORM). *Nat. Methods* (2006) doi:10.1038/nmeth929.
9. Sharonov, A. & Hochstrasser, R. M. Wide-field subdiffraction imaging by accumulated binding of diffusing probes. *Proc. Natl. Acad. Sci. U. S. A.* **103**, 18911–18916 (2006).
10. Valades Cruz, C. A. *et al.* Quantitative nanoscale imaging of orientational order in biological filaments by polarized superresolution microscopy. *Proc. Natl. Acad. Sci. U. S. A.* **113**, (2016).
11. Enderlein, J., Toprak, E. & Selvin, P. R. Polarization effect on position accuracy of fluorophore localization. *Opt. Express* **14**, 8111 (2006).
12. Backlund, M. P., Lew, M. D., Backer, A. S., Sahl, S. J. & Moerner, W. E. The role of molecular dipole orientation in single-molecule fluorescence microscopy and implications for super-resolution imaging. *ChemPhysChem* **15**, 587–599 (2014).
13. Zhang, O. & Lew, M. D. Single-molecule orientation localization microscopy II: a performance comparison. *arXiv* (2020).
14. Zhang, O., Lu, J., Ding, T. & Lew, M. D. Imaging the three-dimensional orientation and rotational mobility of fluorescent emitters using the Tri-spot point spread function. *Appl. Phys. Lett.* **113**, 031103 (2018).
15. Curcio, V., Alemán-Castañeda, L. A., Brown, T. G., Brasselet, S. & Alonso, M. A. Birefringent Fourier filtering for single molecule coordinate and height super-resolution imaging with

dithering and orientation. *Nat. Commun.* **11**, (2020).

16. Lu, J., Mazidi, H., Ding, T., Zhang, O. & Lew, M. D. Single-Molecule 3D Orientation Imaging Reveals Nanoscale Compositional Heterogeneity in Lipid Membranes. *Angew. Chemie Int. Ed.* **59**, 17572–17579 (2020).

17. Toprak, E. *et al.* Defocused orientation and position imaging (DOPI) of myosin V. *Proc. Natl. Acad. Sci. U. S. A.* **103**, 6495–9 (2006).

18. Nevskyi, O., Tsukanov, R., Gregor, I., Karedla, N. & Enderlein, J. Fluorescence polarization filtering for accurate single molecule localization. *APL Photonics* **5**, 061302 (2020).

19. Ding, T., Wu, T., Mazidi, H., Zhang, O. & Lew, M. D. Single-molecule orientation localization microscopy for resolving structural heterogeneities between amyloid fibrils. *Optica* **7**, 602 (2020).

20. Gould, T. J. *et al.* Nanoscale imaging of molecular positions and anisotropies. *Nat. Methods* **5**, 1027–1030 (2008).

21. Forkey, J. N., Quinlan, M. E., Alexander Shaw, M., Corrie, J. E. T. & Goldman, Y. E. Three-dimensional structural dynamics of myosin V by single-molecule fluorescence polarization. *Nature* **422**, 399–404 (2003).

22. Ohmachi, M. *et al.* Fluorescence microscopy for simultaneous observation of 3D orientation and movement and its application to quantum rod-tagged myosin V. *Proc. Natl. Acad. Sci.* (2012) doi:10.1073/pnas.1118472109.

23. Mehta, S. B. *et al.* Dissection of molecular assembly dynamics by tracking orientation and position of single molecules in live cells. *Proc. Natl. Acad. Sci. U. S. A.* **113**, E6352–E6361 (2016).

24. Nordenfelt, P. *et al.* Direction of actin flow dictates integrin LFA-1 orientation during leukocyte migration. *Nat. Commun.* **8**, 2047 (2017).

25. Xu, K., Babcock, H. P. & Zhuang, X. Dual-objective STORM reveals three-dimensional filament organization in the actin cytoskeleton. *Nat. Methods* **9**, 185–188 (2012).

26. Xu, K., Zhong, G. & Zhuang, X. Actin, spectrin, and associated proteins form a periodic cytoskeletal structure in axons. *Science (80-.).* **339**, 452–456 (2013).

27. Van Den Dries, K. *et al.* Dual-color superresolution microscopy reveals nanoscale organization of mechanosensory podosomes. *Mol. Biol. Cell* **24**, 2112–2123 (2013).

28. Whelan, D. R. & Bell, T. D. M. Image artifacts in single molecule localization microscopy: Why optimization of sample preparation protocols matters. *Sci. Rep.* **5**, 1–10 (2015).

29. Bachmann, M., Fiederling, F. & Bastmeyer, M. Practical limitations of superresolution imaging due to conventional sample preparation revealed by a direct comparison of CLSM, SIM and dSTORM. *J. Microsc.* **262**, 306–315 (2016).

30. Leyton-Puig, D. *et al.* PFA fixation enables artifact-free super-resolution imaging of the actin cytoskeleton and associated proteins. *Biol. Open* **5**, 1001–1009 (2016).

31. Heuser, J. E. & Kirschner, M. W. Filament organization revealed in platinum replicas of freeze-dried cytoskeletons. *J. Cell Biol.* **86**, 212–234 (1980).

32. Svitkina, T. M., Verkhovsky, A. B. & Borisy, G. G. Improved procedures for electron microscopic visualization of the cytoskeleton of cultured cells. *J. Struct. Biol.* **115**, 290–303 (1995).

33. Urban, E., Jacob, S., Nemethova, M., Resch, G. P. & Small, J. V. Electron tomography reveals unbranched networks of actin filaments in lamellipodia. *Nat. Cell Biol.* **12**, 429–435 (2010).

34. Svitkina, T. M., Verkhovsky, A. B., McQuade, K. M. & Borisy, G. G. Analysis of the actin-myosin II system in fish epidermal keratocytes: Mechanism of cell body translocation. *J. Cell Biol.* **139**, 397–415 (1997).

35. Schaub, S., Meister, J. J. & Verkhovsky, A. B. Analysis of actin filament network organization in lamellipodia by comparing experimental and simulated images. *J. Cell Sci.* **120**, 1491–1500 (2007).

36. Vinzenz, M. *et al.* Actin branching in the initiation and maintenance of lamellipodia. *J. Cell Sci.* **125**, 2775–2785 (2012).

37. Enderlein, J. *et al.* Polarization effect on position accuracy of fluorophore localization. *J. D. Jackson Class. Electrodyn. Phys. Lett* **14**, 337–350 (2006).

38. Lew, M. D., Backlund, M. P. & Moerner, W. E. Rotational Mobility of Single Molecules Affects Localization Accuracy in Super-Resolution Fluorescence Microscopy. *Nano Lett.* **13**, 3967–3972 (2013).

39. Wulf, E., Deboben, A., Bautz, F. A., Faulstich, H. & Wieland, T. Fluorescent phallotoxin, a tool for the visualization of cellular actin. *Proc. Natl. Acad. Sci. U. S. A.* **76**, 4498–4502 (1979).

40. Barak, L. S., Rogers Yocum, R., Nothnagel, E. A. & Webb, W. W. Fluorescence staining of the actin cytoskeleton in living cells with 7-nitrobenz-2-oxa-1,3-diazole-phallacidin. *Proc. Natl. Acad. Sci. U. S. A.* **77**, 980–984 (1980).

41. Oda, T., Namba, K. & Maéda, Y. Position and orientation of phalloidin in F-actin determined by x-ray fiber diffraction analysis. *Biophys. J.* **88**, 2727–2736 (2005).

42. Tojkander, S., Gateva, G. & Lappalainen, P. Actin stress fibers – assembly, dynamics and biological roles. *J. Cell Sci.* **125**, 1855–1864.

43. Vallenius, T. Actin stress fibre subtypes in mesenchymal-migrating cells. *Open Biol.* **3**, 130001 (2013).

44. Tojkander, S., Gateva, G., Husain, A., Krishnan, R. & Lappalainen, P. Generation of contractile actomyosin bundles depends on mechanosensitive actin filament assembly and disassembly. *Elife* (2015) doi:10.7554/eLife.06126.001.

45. Hu, S. *et al.* Long-range self-organization of cytoskeletal myosin II filament stacks. *Nat. Cell Biol.* **19**, 133–141 (2017).

46. Fenix, A. M. *et al.* Expansion and concatenation of nonmuscle myosin IIA filaments drive cellular contractile system formation during interphase and mitosis. *Mol. Biol. Cell* **27**, 1465–1478 (2016).

47. Vignaud, T. *et al.* Stress fibres are embedded in a contractile cortical network. *Nat. Mater.* (2020) doi:10.1038/s41563-020-00825-z.

48. Revach, O. Y., Grosheva, I. & Geiger, B. Biomechanical regulation of focal adhesion and invadopodia formation. *Journal of cell science* vol. 133 (2020).

49. Kanchanawong, P. *et al.* Nanoscale architecture of integrin-based cell adhesions. *Nature* **468**, 580–584 (2010).

50. Tanner, K., Boudreau, A., Bissell, M. J. & Kumar, S. Dissecting regional variations in stress fiber mechanics in living cells with laser nanosurgery. *Biophys. J.* (2010)

doi:10.1016/j.bpj.2010.08.071.

51. Hotulainen, P. & Lappalainen, P. Stress fibers are generated by two distinct actin assembly mechanisms in motile cells. *J. Cell Biol.* **173**, 383–394 (2006).

52. Svitkina, T. M. & Borisy, G. G. Arp2/3 complex and actin depolymerizing factor/cofilin in dendritic organization and treadmilling of actin filament array in lamellipodia. *J. Cell Biol.* **145**, 1009–1026 (1999).

53. Verkhovsky, A. B. *et al.* Orientational Order of the Lamellipodial Actin Network as Demonstrated in Living Motile Cells. *Mol. Biol. Cell* **14**, 4667–4675 (2003).

54. Mueller, J. *et al.* Load Adaptation of Lamellipodial Actin Networks. *Cell* **171**, 188-200.e16 (2017).

55. Koestler, S. A., Auinger, S., Vinzenz, M., Rottner, K. & Small, J. V. Differentially oriented populations of actin filaments generated in lamellipodia collaborate in pushing and pausing at the cell front. *Nat. Cell Biol.* **10**, 306–313 (2008).

56. Weichsel, J., Urban, E., Small, J. V. & Schwarz, U. S. Reconstructing the orientation distribution of actin filaments in the lamellipodium of migrating keratocytes from electron microscopy tomography data. *Cytom. Part A* (2012) doi:10.1002/cyto.a.22050.

57. Weichsel, J., Urban, E., Small, J. V. & Schwarz, U. S. Reconstructing the orientation distribution of actin filaments in the lamellipodium of migrating keratocytes from electron microscopy tomography data. *Cytom. Part A* **81A**, 496–507 (2012).

58. Spira, F. *et al.* Cytokinesis in vertebrate cells initiates by contraction of an equatorial actomyosin network composed of randomly oriented filaments. (2017) doi:10.7554/eLife.30867.001.

59. Nakai, N. *et al.* Genetically encoded orientation probes for F-actin for fluorescence polarization microscopy. *Microscopy* **68**, 359–368 (2019).

60. Manley, S., Gillette, J. M. & Lippincott-Schwartz, J. Single-Particle Tracking Photoactivated Localization Microscopy for Mapping Single-Molecule Dynamics. doi:10.1016/S0076-6879(10)75005-9.

61. Huang, B., Wang, W., Bates, M. & Zhuang, X. Three-dimensional super-resolution imaging by stochastic optical reconstruction microscopy. *Science* **319**, 810–3 (2008).

62. Juette, M. F. *et al.* Three-dimensional sub-100 nm resolution fluorescence microscopy of thick samples. *Nat. Methods* **5**, 527–529 (2008).

63. Abrahamsson, S. *et al.* MultiFocus Polarization Microscope (MF- PolScope) for 3D polarization imaging of up to 25 focal planes simultaneously. doi:10.1364/OE.23.007734.

64. Chakraborty, S., Jasnin, M. & Baumeister, W. Three-dimensional organization of the cytoskeleton: A cryo-electron tomography perspective. *Protein Sci.* **29**, 1302–1320 (2020).

4polar-STORM polarized super-resolution imaging of actin filament organization in cells

Caio Vaz Rimoli[1,&], Cesar Augusto Valades Cruz[2,3,&], Valentina Curcio[1], Manos Mavrakis[1,*], Sophie Brasselet[1,*]

1 Aix Marseille Univ, CNRS, Centrale Marseille, Institut Fresnel, F-13013 Marseille, France

2 Institut Curie, PSL Research University, UMR144 CNRS, Space-Time imaging of organelles and Endomembranes Dynamics Team, F-75005, Paris, France

3 Inria Centre Rennes-Bretagne Atlantique, SERPICO Project Team, F-35042, Rennes, France

[&] these authors contributed equally to the work

* corresponding authors contact : sophie.brasselet@fresnel.fr, manos.mavrakis@univ-amu.fr

Content

Supplementary Note 1. Model and retrieval of orientation parameters

A single molecule orientation is determined by its absorption dipole $\vec{\mu}_a$ and emission dipole $\vec{\mu}_e$, which lie along transition dipole moment directions for the respective absorption and emission transitions. In what follows, we suppose that the absorption and emission dipoles have the same orientation. This assumption is appropriate in the present work which focuses on the emission detection only, but different situations can also be derived from the following equations.

Dipole orientations (θ, φ) are defined in the frame of the distribution angles that the molecule explores during the integration time of the image (typically tens to hundreds ms, which is much longer than the rotational time of the molecules). We consider a molecule wobbling within a distribution $f(\theta, \varphi)$ during the integration time of the detector. $f(\theta, \varphi)$ is defined here as a cone function, of value 1 for $(0 \leq \theta \leq \delta/2)$ and 0 elsewhere (a Gaussian function would lead to very similar results). ρ is the orientation of the projection of the cone in the sample plane (x, y), and η is the out-of-plane orientation of the cone, relative to z (see Figure).
The absorption and emission dipoles $\vec{\mu}_a(\theta, \varphi)$ and $\vec{\mu}_e(\theta, \varphi)$ are therefore expressed in the macroscopic frame (x, y, z) of the sample as:

$$\vec{\mu}_{a,e}(\theta, \varphi, \rho, \eta) = \mu_{a,e} \begin{bmatrix} \sin^2\rho + \cos\eta\cos^2\rho & (\cos\eta - 1)\sin\rho\cos\rho & \sin\eta\cos\rho \\ (\cos\eta - 1)\sin\rho\cos\rho & \cos^2\rho + \cos\eta\sin^2\rho & \sin\eta\sin\rho \\ -\sin\eta\cos\rho & -\sin\eta\sin\rho & \cos\eta \end{bmatrix} \begin{bmatrix} \sin\theta\cos\varphi \\ \sin\theta\sin\varphi \\ \cos\theta \end{bmatrix}$$

Eq. S1

Where $\mu_{a,e}$ is the dipole amplitude.

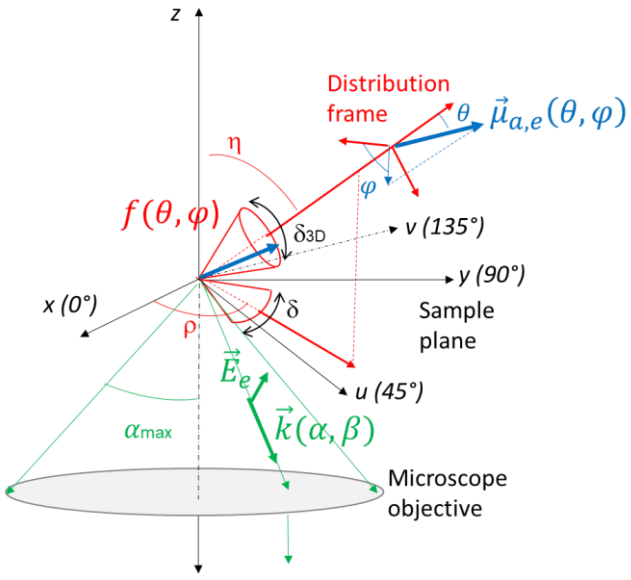

The fluorescence signal is the result of an excitation step, whose efficiency is quantified by the absorption probability, and an emission step, in which the emission dipole radiates. A complete derivation of the fluorescence signal from wobbling dipoles can be found for instance in[1]. Here we provide the expressions used in this work to extract the orientation parameters from single dipoles, from polarized intensities measured in the 4polar-STORM method.

Excitation. The absorption probability is proportional to[2]:

$$P_{abs}(\theta,\varphi,\rho,\eta) \propto \left|\vec{\mu}_a(\theta,\varphi,\rho,\eta)\cdot\vec{E}\right|^2 \qquad \text{Eq. S2}$$

with $\vec{E}$ the excitation field.

In the case of normal incidence circular polarization, $\vec{E} = E_0(1,1,0)$ with E_0 the field amplitude.

In the case of total internal reflection (TIRF) illumination, $\vec{E} = \left(E_x, E_y, E_z\right)$ takes a more complex form that can be found in[3], which involves a contribution along z. In the present work, the incident polarization in TIRF is set such as the in-plane $\left(E_x, E_y\right)$ contributions are balanced, in order to minimize any in-plane photoselection.

Emission. The emission field radiated from the emission dipole $\vec{\mu}_e$ along the propagation direction $\vec{k}$ writes, in free space:

$$\vec{E}_e(\theta,\varphi,\rho,\eta,\vec{k}) \propto (\vec{k}\times\vec{\mu}_e(\theta,\varphi,\rho,\eta))\times\vec{k} \qquad \text{Eq. S3}$$

In reality the dipole is placed within a medium of refractive index supposedly close to water, above an interface with glass. To account for these interfaces, expressions derived in[4] and[5] are used.

Fluorescence intensity. The fluorescence intensity detected along a polarization direction $\vec{\varepsilon}$ and a propagation vector $\vec{k}$ (see Figure) is deduced from the absorption and emission probabilities product[2,6,7]:

$$I_\varepsilon(\vec{k}) \propto \int_0^{2\pi} d\varphi \int_0^{\delta/2} d\theta \ \sin\theta\, P_{abs}(\theta,\varphi)\left|\vec{E}_e\left(\theta,\varphi,\rho,\eta,\vec{k}\right)\cdot\vec{\varepsilon}\right|^2 \qquad \text{Eq. S4}$$

Where $\propto$ encompasses all collection/excitation efficiency factors that do not affect the present analysis. To account for the detection numerical aperture (NA), it is necessary to integrate all vector fields directions $\vec{k}(\alpha,\beta)$ over the collected NA, with $(0 \le \alpha \le \alpha_{max}, 0 \le \beta \le 2\pi)$. The total detected intensity writes therefore as:

$$I_\varepsilon = \int_0^{2\pi} d\beta \int_0^{\alpha_{max}} d\alpha \ \sin\alpha\, I_\varepsilon(\vec{k}(\alpha,\beta)) \qquad \text{Eq. S5}$$

Which means that at high NA integration, the detection is affected by a mixture of polarization contributions.

A simplified writing of this integration is[8]:

$$I_\varepsilon = \kappa_1 I_\varepsilon + \kappa_2 I_{\varepsilon_\perp} + \kappa_3 I_z$$

with $(\vec{\varepsilon}, \vec{\varepsilon}_\perp, \vec{z})$ forming a direct orthonormal basis (in this work, either (x,y,z) or (u,v,z)) and with the $(\kappa_1,\kappa_2,\kappa_3)$ coefficients follow a specific dependence on the NA [8]:

$$\kappa_3 = \frac{1}{3}(2 - 3\cos\alpha_{max} + \cos^3\alpha_{max})$$
$$\kappa_2 = \frac{1}{12}(1 - 3\cos\alpha_{max} + 3\cos^2\alpha_{max} - \cos^3\alpha_{max})$$
$$\kappa_1 = \frac{1}{4}(5 - 3\cos\alpha_{max} - \cos^2\alpha_{max} - \cos^3\alpha_{max})$$

In this work, the detection is performed along the polarization directions (0°, 90°, 45°, 135°), e.g. $\vec{\varepsilon} = \vec{x}, \vec{y}, \vec{u}, \vec{v}$ with $\vec{u} = (\vec{x} + \vec{y})/\sqrt{2}$ and $\vec{v} = (\vec{y} - \vec{x})/\sqrt{2}$. Equations S4, S5 show that there is a matrix relation between the measured intensities $(I_0, I_{90}, I_{45}, I_{135})$ and the dipole-orientation dependent quantities:

$$\langle \mu_{e,\varepsilon} \cdot \mu^*_{e,\varepsilon'} \rangle(\rho, \delta, \eta) = \int_0^{2\pi} d\varphi \int_0^{\delta/2} d\theta \ \sin\theta \, P_{abs}(\theta, \varphi) \, \mu_{e,\varepsilon}(\theta, \varphi, \rho, \eta) \cdot \mu^*_{e,\varepsilon'}(\theta, \varphi, \rho, \eta)$$

Eq. S6

with $(\varepsilon, \varepsilon')$= (x, y, z).

To measure the molecular orientation parameters (ρ, δ) with the condition $(\eta = 90°)$, two independent measurements are required. Note that η cannot be extracted from a 4polar-STORM measurement unless specific defocusing or interface-imaging conditions are realized which involve PSF fitting[1,9]. The present work is based on ratiometric intensity imaging, which does not require any PSF fitting. We define the two polarization factors, normalized with respect to the total intensity:

$$P_0 = \frac{I_0 - I_{90}}{I_0 + I_{90}} \quad \text{and} \quad P_{45} = \frac{I_{45} - I_{135}}{I_{45} + I_{135}}$$

Eq. S7

We denote the total intensity $I_T = I_0 + I_{90} + I_{45} + I_{135}$. Note that $I_0 + I_{90} = I_{45} + I_{135}$ in an ideal optical system.

From the measurements of the intensities $(I_0, I_{90}, I_{45}, I_{135})$ or the ratios (P_0, P_{45}), components $\langle \mu_{e,\varepsilon} \cdot \mu^*_{e,\varepsilon'} \rangle(\rho, \delta)$ with $(\varepsilon, \varepsilon') = (x, x), (y, y), (x, y)$ can be retrieved. These quantities depend on the orientation parameters (ρ, δ). Note that this measurement is an in-plane projection of polarizations, and is therefore insensitive to components involving z, e.g. the 3D orientation η of the emission dipoles.

A very simple expression of the moments expressed in Eq. S6 can be given ignoring the 3D expansion of the cone distribution (e.g. $f(\theta, \varphi)$ is a 2D-flat cone $(\theta \in [0, \delta/2], \varphi \in [0, 2\pi])$. Supposing no photoselection along the in-plane excitation directions, which is achievable experimentally, this dependence is:

$$\langle \mu_{e,x} \cdot \mu^*_{e,x} \rangle(\rho, \delta) = \frac{\mu_e^2}{2}(\cos 2\rho \ \mathrm{sinc}\, \delta + 1)$$
$$\langle \mu_{e,y} \cdot \mu^*_{e,y} \rangle(\rho, \delta) = \frac{\mu_e^2}{2}(1 - \cos 2\rho \ \mathrm{sinc}\, \delta)$$
$$\langle \mu_{e,x} \cdot \mu^*_{e,y} \rangle(\rho, \delta) = \mu_e^2(\sin 2\rho \ \mathrm{sinc}\, \delta)$$

Eq. S8

The (ρ, δ) parameters can easily be extracted from Eq. S8.

Inspired from this derivation, a simplified procedure is developed to analyse 4polar-STORM images. The (ρ, δ) parameters retrieval is made under the assumption that the molecular wobbling distribution lies within the sample plane with $(\eta = 90°)$. We consider also that there is no specific photoselection between the x and y (a z contribution of the excitation field in the absorption probability can be possibly introduced if using TIRF). Under the paraxial approximation for the detection, the fluorescence intensity along the detection polarization, for an emission dipole $\vec{\mu}_e(\theta, \varphi)$ oriented along (θ, φ), can then be simplified into:

$$I_\varepsilon(\theta, \varphi, \rho, \eta) \propto |\vec{\mu}_e(\theta, \varphi, \rho, \eta) \cdot \vec{\varepsilon}|^2 \qquad \text{Eq. S9}$$

with $\vec{\varepsilon} = \vec{x}\ (I_0), \vec{y}\ (I_{90}), \vec{u}\ (I_{45}), \vec{v}\ (I_{135})$, with $\vec{u} = (\vec{x} + \vec{y})/\sqrt{2}$ and $\vec{v} = (\vec{y} - \vec{x})/\sqrt{2}$.
Simplifying the cone distribution function into a 2D-flat cone $(\theta \in [0, \delta/2], \varphi \in [0,2\pi])$, the integration over the distribution function simplifies the detected intensities into :

$$I_0 = \frac{I_T}{2}(\cos 2\rho\ \mathrm{sinc}\,\delta + 1) \text{ and } I_{90} = \frac{I_T}{2}(1 - \cos 2\rho\ \mathrm{sinc}\,\delta)$$
$$I_{45} = \frac{I_T}{2}(\sin 2\rho\ \mathrm{sinc}\,\delta + 1) \text{ and } I_{135} = \frac{I_T}{2}(1 - \sin 2\rho\ \mathrm{sinc}\,\delta) \qquad \text{Eq. S10}$$

With $\mathrm{sinc}\,\delta = \frac{\sin\delta}{\delta}$ and I_T the total intensity.
Under these conditions,

$$P_0(\rho, \delta) = \cos 2\rho\ \mathrm{sinc}\,\delta$$
$$P_{45}(\rho, \delta) = \sin 2\rho\ \mathrm{sinc}\,\delta \qquad \text{Eq. S11}$$

Therefore the orientation parameters can be easily deduced with

$$\rho = \frac{1}{2}\ \mathrm{atan}\left(\frac{P_{45}}{P_0}\right)$$
$$\mathrm{sinc}\,\delta = \sqrt{P_0^2 + P_{45}^2} \qquad \text{Eq. S12}$$

These expressions will be used to analyse the 4polar-STORM results, and their validity in real situations (high detection NA, tilted wobbling distribution) is discussed below. Importantly, Eq. S12 shows that the 4polar-STORM method permits to estimate ρ and δ independently, which is not the case of polarization schemes that use only two polarization projections[10].

Equation S12 is valid for wobbling molecules lying in a flat cone in the sample plane and in the paraxial approximation. When molecular distributions resemble a full cone tilted off-plane $(\eta < 90°)$, the determined ρ parameter is expected to be unchanged, however δ will be overestimated. This overestimation is expected to be even more dramatic when η decreases away from 90° and when working at high NA, since the emission of highly tilted dipoles is mostly manifested at high NA, e.g. highly tilted $\vec{k}$ vectors[11]. The bias between the expected δ (denoted δ_{3D}) and the measured δ

(extracted from Eq. S12) is represented in Fig. S1 for different tilt angles η of the cone distribution representing the molecular wobbling. To calculate this bias, expressions of the polarized intensities $(I_0, I_{90}, I_{45}, I_{135})$ are extracted from Eq. S5 using the TIRF illumination condition used in this work, and generating different sets of calculated (η, δ) parameters, supposing $\rho = 0°$ (this parameter does not influence the results). From these intensities, δ is determined using Eq. S12. The results show that at the working condition NA = 1.45, a strong bias on δ is visible even in wobbling cones lying in the sample plane ($\eta = 90°$). This bias is however strongly reduced when reducing the detection NA, which reduces the detection efficiency of tilted dipoles. At NA = 1.2, the bias on δ stays at reasonable level for δ values measured in this work ($\delta \sim 90°$), as long as $\eta > 45°$ while keeping a reasonable signal to noise condition (about 60% of the total intensity is preserved for cones lying close to the sample plane with $\eta > 45°$). In order to provide an unbiased picture of δ values for in-plane lying wobbling cones, it is thus favourable to work at a detection NA close to 1.2.

The use of the 'flat cone' model used in Eq. S12 is shown to allow a close to unbiased determination of δ when the cone is lying in the sample plane (Fig. S1). The reason for this is that molecules are essentially excited in the sample plane, which decreases the weight of molecules possibly oriented off-plane in the final polarized intensities. The difference between the 'flat cone' model used in Eq. S12 and the full cone model has been assessed more precisely by evaluating the effect of each model on the quantity $\left(P_0^2 + P_{45}^2\right)$ determined for the estimation of the orientation parameters (see Eq. S12). Figure S2 shows the difference of values obtained in both models. It is found that this model can be reasonably used with typical differences of 10% found on $\left(P_0^2 + P_{45}^2\right)$ for $\delta \sim 100°$.

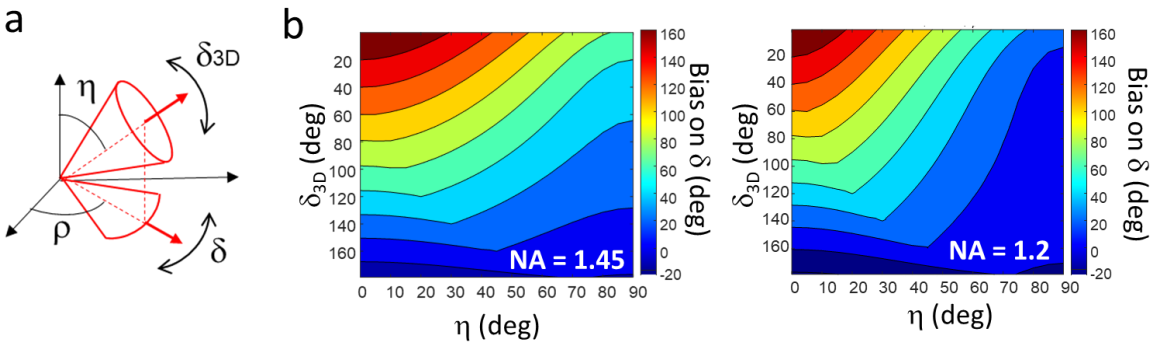

Figure S1. Retrieval bias on δ. (a) Schematic representation of a single molecule oriented in 3D by the mean orientation angles (ρ,η) and a wobbling cone angle of δ_{3D}. The measured wobbling in 2D is δ. (b) Bias on δ (difference between the measured δ and the true value δ_{3D}), under TIRF illumination and different detection NA conditions, as a function of the molecule tilt angle η (depicted in (a)).

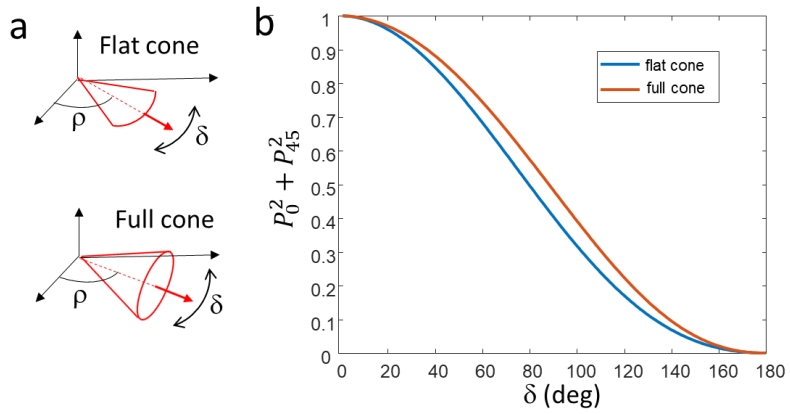

Figure S2. Cone model used for orientation parameter retrieval. (a) Approximated 2D 'flat cone' model used for the parameter retrieval, compared to a 'full cone' model. (b) The used parameter $P_0^2 + P_{45}^2$ for the retrieval of δ is depicted as a function of δ, in the case of a full cone model (red) and a flat cone model (blue). The difference between both models reaches 10% at δ = 100°.

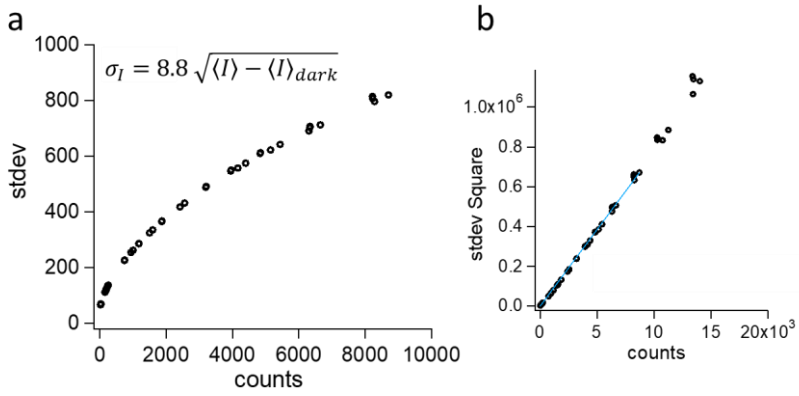

Figure S3. Camera noise estimation. (a) Dependence of the standard deviation σ_I of the measured signal with respect to its mean value $\langle I \rangle$, measured on 500 samples (image regions of interest), using a camera gain of 300. The measurement was performed on homogeneous images produce by white light illumination of a piece of paper. Markers: experimental data. (b) Same data represented as σ_I^2. Blue line: linear fit, found to be of slope 77.5. The equation $\sigma_I = 8.8\sqrt{I - I_{dark}}$, is thus used as a noise model for the used camera in the present working conditions. An offset of $I_{dark} = 480$ counts is systematically removed to account for the camera electronic dark counts, irrespectively of the gain and exposure time. This offset is subtracted from all data acquisitions, including calibrations. The linearity of the camera response was moreover validated in the range of signals typically measured.

Supplementary Information Note 2. Calibration factors in 4polar-STORM

Due to imperfections of the beam splitters as well as possible polarization leakages introduced by the optics of the detection path, correction factors need to be introduced in the estimation of the

polarization factors P_0 and P_{45}. We denote G_{BS} the factor accounting for the imperfect 50:50 reflection:transmission ratio of the first non-polarizing beam splitter. We also denote G_0 and G_{45} the factors accounting for the unbalanced polarization split efficiency in the 0:90 and the 45:135 polarization channels respectively. (G_{BS}, G_0, G_{45}) are measured using a depolarized image (fluorescent solution) in which the ratios write:

$$G_{BS} = \frac{I_{45}+I_{135}}{I_0+I_{90}}\,;\, G_0 = \frac{I_0}{I_{90}}\,;\, G_{45} = \frac{I_{45}}{I_{135}} \qquad \text{Eq. S13}$$

We also account for possible polarization leakages between the 0:90 and 45:135 channels. The contributions are measured by polarizing the previous un-polarized image using a polarizer of known direction at the position of the back focal plane of the objective, before propagation through the dichroic filter and other propagation optics. This is performed using a controlled polarizer direction at the back focal objective plane (thin polarizer used, LPVISE100-A, Thorlabs). Denoting G_1 (resp. G_2) the leakage proportion factor of polarization channel 135° (resp. 45°) into the 45° channel (resp. 135°), and G'_1 (resp. G'_2) for the 0°/90° leakage, the final corrected expressions are:

$$P_0 = G_{BS} \cdot \frac{(1+G'_1-G'_2)\cdot I_0 - (1-G'_1+G_2)\cdot G_0 \cdot I_{90}}{(1-G'_1-G'_2)\cdot (I_0 + G_0.I_{90})}$$

$$P_{45} = \frac{(1+G_1-G_2)\cdot I_{45} - (1-G_1+G_2)\cdot G_{45}\cdot I_{135}}{(1-G_1-G_2)\cdot (I_{45} + G_{45}.I_{135})}$$

Eq. S14

In an ideal optical system, $G_{BS} = G_0 = G_{45} = 1$ and $G_1 = G_2 = G'_1 = G'_2 = 0$. Deviations up to 0.2 from these numbers can be found in a real setup.

Supplementary Information Note 3. Data processing algorithm of the 4polar-STORM method

The data processing is achieved by custom detection and analysis scripts written in Matlab, following a scheme summarized below. The scripts are based on previous work published in[10]. The previous polar-STORM algorithm, written for a two-image polarization split, has been adapted to a split into four images named (*img$_0$, img$_{45}$, img$_{90}$, Img$_{135}$*). Its goal is to estimate the polarization factors P_0 and P_{45} for each detected single molecule, build a super-resolved image of these polarization factors, and reconstruct an orientation super-resolved image from them. The purpose of the 4polar-STORM algorithm is thus to retrieve, per molecule, its center point spread function (PSF) position coordinates in the 4 detected images (i_0, i_{45}, i_{90}, i_{135}), (j_0, j_{45}, j_{90}, j_{135}), its PSF radius (r_0, r_{45}, r_{90}, r_{135}), its localization precision ($\sigma_{loc,0}$, $\sigma_{loc,45}$, $\sigma_{loc,90}$, $\sigma_{loc,135}$) and its PSF amplitude (α_0, α_{45}, α_{90}, α_{135}), used to calculate the intensities (I_0, I_{45}, I_{90}, I_{135}) and thus the polarization factors P_0 and P_{45} (see Eq. S7). Once these two factors are calculated, we deduce the orientation parameters for each single molecule (in-plane orientation angle ρ and wobbling angle value δ) using Eq. S12. This algorithm offers advantages as compared to a pure ratiometric calculation based on image registration, since the pairing is realized at

the molecular level for each STORM stack recorded, without any requirement of pre-calibration experiment which may add additional positioning errors and therefore bias in the polarization factor estimation. This algorithm contains several sequential steps detailed below.

Distortion correction. A calibration sample (fluorescent nanobeads) is used to correct images from distortions. Fluorescent nanobeads of 100 nm in size (yellow-green Carboxylate-Modified FluoSpheres, ThermoFisher Scientific F8803) are immobilized on the surface of a poly-L-lysine coated coverslip and covered with a mounting medium (Fluoromount, Sigma F4680). A Fluorescent nanobeads image is used to estimate the spatial transformation (*tform*) to be used between the different polarization projections to correct any possible geometrical distortion, due mainly to the use of Wollaston prisms. We selected the quadrant img_{90} as the reference image for the registration. The function *imregtform* (Matlab Imaging Processing toolbox) was used to retrieve the *tform* function for the other three quadrants (img_0, img_{45} *and* Img_{135}). Then we correct these images using the transformation previously estimated. The spatial transformation was re-calculated only if the optical setup was modified. The correction was performed using the Matlab function *imwarp* under a linear interpolation (Matlab Imaging Processing toolbox).

Detection and estimation. As in the polar-STORM algorithm[10], single molecule localizations in image quadrants (img_0, img_{45}, img_{90}, Img_{135}) are based on a first detection step which uses a Generalized likelihood ratio test (GLRT) to identify the single molecule candidates for the STORM image reconstruction, as detailed in[12]. This detection step uses a given fixed Gaussian shape for the theoretical PSF (starting from an initial guess radius of r = 1.3 pixels), a spatial sliding detection window (w_s) and a limit probability of false alarm (PFA)[12], which defines a threshold limit (calculated empirically based on Monte Carlo simulations) above which any signal can be statistically considered as having a different origin than noise. A value PFA ≤ 10^{-6} is set to guarantee a probability of false alarm (PFA) of less than 1 pixel per image, which ensures a fraction of the detected single molecules close to 100% for a signal to noise ratio (SNR) higher than 20dB[12]. After the candidates have been detected by the GLRT algorithm, the amplitude, radius and position of their Gaussian PSF are estimated on all four quadrants at the subpixel level, based on a Maximum likelihood (ML) estimation using a Gauss-Newton regression. This regression uses the GRLT obtained values of radius and position as initial parameters. The localization accuracy (σ_{loc}) is estimated from a computation of the Cramer-Rao bound (CRB) limit[12], and given for all quadrant images.

Estimation of the translation vector between image quadrant pairs: (img_0 - img_{90}), (img_{45} - Img_{135}) and (img_0 - img_{45}). To estimate the translation vector between the different images and associate each detected PSF to a given molecule, it is possible to use the registration from the bead sample used for the distortion-correction step above. This type of registration is however limited by the camera pixel size, image quality and stability of the optical system. It also implies the use of interpolation methods during the image subsampling. The 4polar-STORM software rather directly calculates the translation vector using the detected molecules themselves, which are localized with high precision. The distance of each molecules' images in the quadrant pairs *(img_0 - img_{90}), (img_{45} - Img_{135}),* and *(img_0 - img_{45})* created by the Wollaston polarization beam splitter prisms is represented by three vectors ($\vec{u}_{0-90}$, $\vec{u}_{45-135}$, $\vec{u}_{0-45}$). The knowledge of these translational vectors is required for the detection of the molecule-pairs present in a STORM image stack. To estimate the vectors, we perform a statistical estimation by using the 100-1,000 first frames of the STORM recorded stack[10]. First, all possible vectors joining two molecules of the images are calculated and the squared norms of the differences between

all the obtained vectors are calculated. This leads to a statistical distribution, within which only the candidates whose difference is below 4.2 times the obtained standard deviation are kept (pure significant test assuming that the difference between norms follows a Gaussian distribution, which guarantees a 95% confidence level to have similar directions between the selected pairs of PSF images). Second, an additional selection is performed to determine the most optimal vector. This second step compares the obtained vector squared-norms and keeps the largest ensemble of similar squared-norms in this population. For this a sub-optimal detection is run (the only hypothesis being that the error on position is Gaussian), keeping errors only below a threshold that guaranties a 95% confidence level within the obtained distribution.

Association of molecule pairs. After the three optimal vectors ($\vec{u}_{0-90}$, $\vec{u}_{45-135}$, $\vec{u}_{0-45}$) are calculated, pairs of molecules along these directions are coupled by selecting the nearest neighbor to the expected position at a vector distance from the reference quadrant, within a distance tolerance corresponding to the localization precision. First, molecules from the images pairs (img_0 - img_{90}) and (img_{45} - img_{135}) are coupled separately over the full STORM stack (typically 30 000 – 50 000 images), then the identified couples are associated using $\vec{u}_{0-45}$.

Estimation of molecular parameters. The pairing of all molecules allows the reconstruction of a polarization STORM image based on the parameter position (i_0, i_{45}, i_{90}, i_{135}), (j_0, j_{45}, j_{90}, j_{135}), PSF radius (r_0, r_{45}, r_{90}, r_{135}), localization precision ($\sigma_{loc,0}$, $\sigma_{loc,45}$, $\sigma_{loc,90}$, $\sigma_{loc,135}$) and PSF amplitude (α_0, α_{45}, α_{90}, α_{135}). Only molecules that were presented in all four-quadrants were considered for analysis to avoid bias in the orientation and intensity estimation.

Calculation of polarization factors P_0 and P_{45}. Polarization factors P_0 and P_{45} (see Supplementary Note 1) are calculated based on the integrated intensities I_0, I_{45}, I_{90} and I_{135}, which are calculated from (α_0, r_0), (α_{45}, r_{45}), (α_{90}, r_{90}) and (α_{135}, r_{135}):

$$I = 2\sqrt{\pi} r \alpha \qquad \text{Eq. S15}$$

After intensities are estimated, the polarization factors (P_0, P_{45}) are deduced, accounting for the calibration correction factors as detailed in Eq. S14 (see Supplementary Note 2).

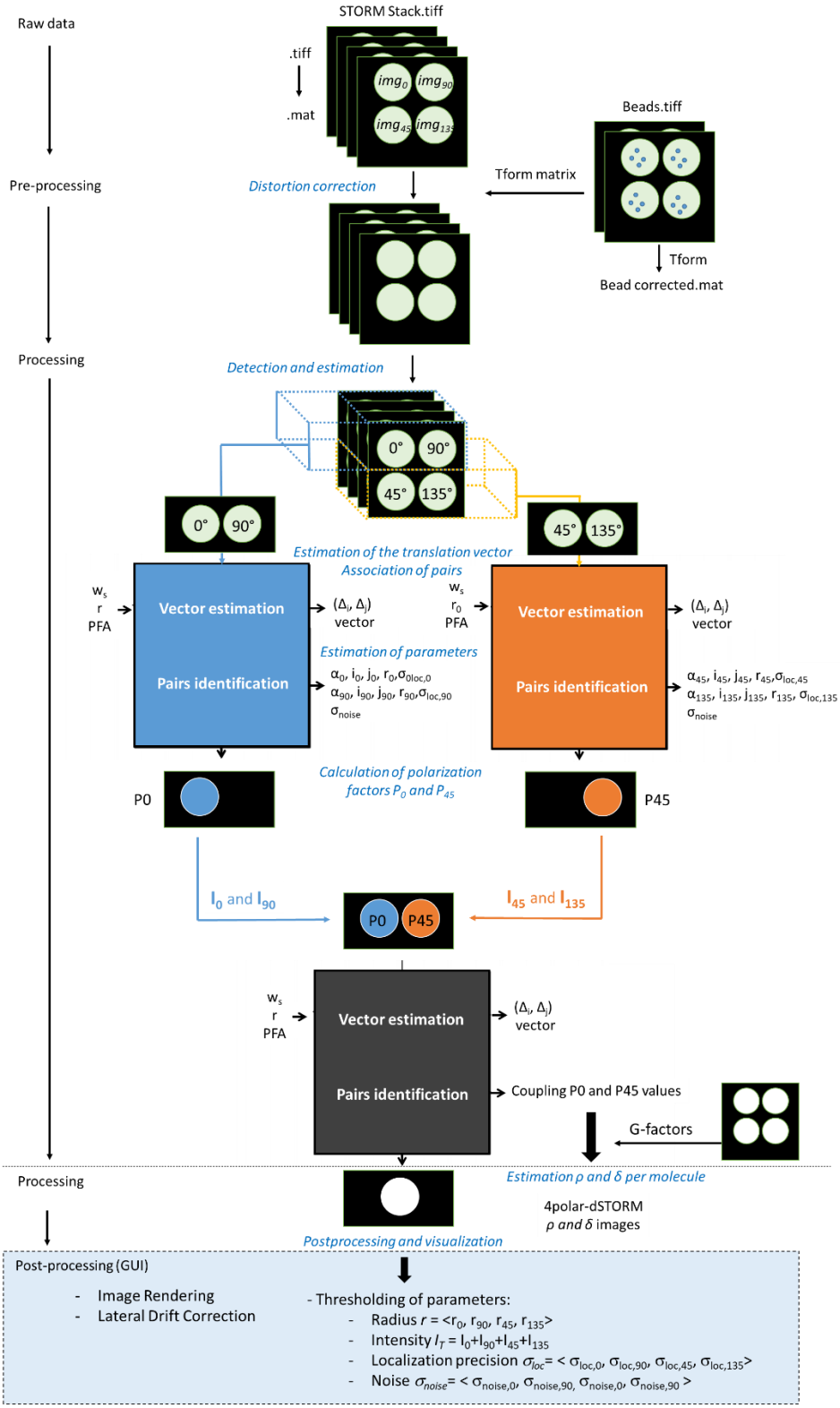

4polar-STORM algorithm flowchart. In the pre-processing step, the raw data (.tiff image stack files) is transformed into ".mat" files to be further spatially corrected by the bead calibration in Matlab. The distortion-corrected stack files are processed for each Wollaston polarized arm (in blue, the pair 0°-90°, and in orange, the pair 45°-135°). On each arm, the 4polar-STORM algorithm is applied: GLRT is applied to find the best translation vector, which is further used to identify coupled blinking pair

events. A multi-parametric Gaussian-Newton fit is performed to retrieve quantitative parameters of the blinking particles, such as position (i,j), localization precision (σ_{loc}), the amplitude (α), radius (r), and noise (σ_{noise}). A vector estimation and pair identification (coupling) is done to group the information into polarization factor ratios P0 and P45. The last step of the data treatment is to calculate the orientation parameters for each blinking particle in the reconstructed image. For that, the G-factors (i.e., the intensity calibration correction) are applied. Post-processing is performed using a derivation of PALMSiever[13]. The most common post-processing steps used for 4polar-STORM are: (1) lateral drift correction (based on cross-correlation with the localization themselves), (2) choice of image rendering, (3) parameter thresholding for robust orientation parameter estimation, and (4) choice of the stick representation.

Estimation of ρ and δ per molecule. After the polarization factors are calculated, *ρ* and *δ* are estimated based on the expressions given in Eq. S12. To solve the determination of *δ,* an interpolation is performed using the function "*interp1*" of Matlab.

Postprocessing and visualization. Postprocessing is performed in a modified version of PALMsiever[13], a visualization and analysis platform for single-molecule localization microscopy implemented in Matlab. It uses the software package DIPimage (https://diplib.org/DIPimage). PALMsiever includes a plugin for drift correction using cross-correlation. For this work, we used two rendering modalities: histogram + Gaussian filter and Kernel Density Estimation (KDE)[14]. KDE is a smoothing version of histogram, with the smoothing kernel bandwidth estimated from the molecule density. Our version of PALMsiever of the 4polar-STORM modality includes the estimation of *ρ* and *δ*, as well as their graphical representation as sticks. In this representation, *ρ* is depicted as the orientation angle of sticks (with respect to the horizontal axis of the image), and δ or *ρ* are depicted as the colors of the sticks. The sticks are displayed over a black-and-white image representing the super-resolved STORM image, which uses the localization of all detected molecules. 4polar-STORM allows to use the default parameter filters of PALMsiever for the image representation, filtering for instance molecule populations by their density, intensity and localization precision. An example of 4polar-STORM representation is shown below.

Representation of ρ and δ in STORM images. The final 4polar-STORM representation consists in depicting, over a STORM image background, one stick per single molecule detected, whose orientation relative to the horizontal axis is *ρ,* and whose color is either encoding *ρ* or *δ*. In the chosen representation, we plot sticks with largest *δ* values above sticks with lowest ones, in order to better visualize the presence of highly wobbling populations in red.

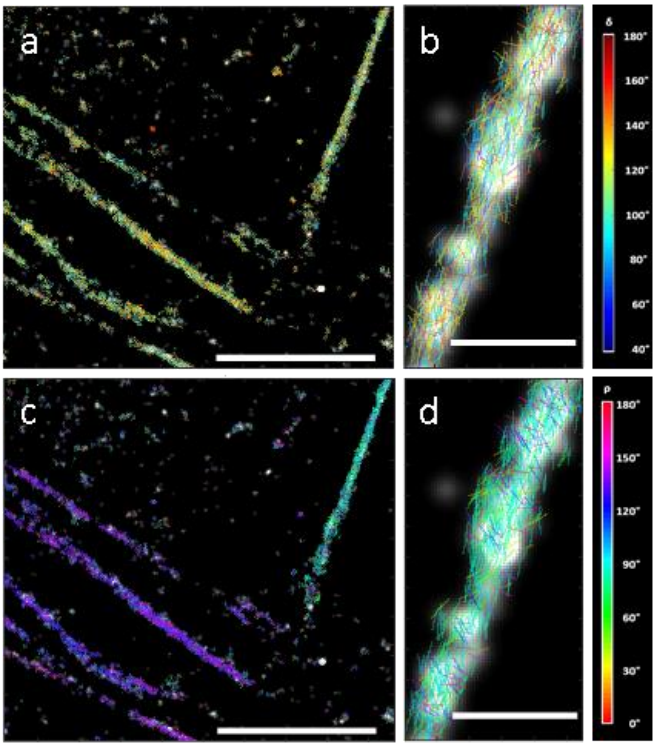

4polar-STORM stick representations of (δ,ρ). Example of super-resolved image of δ (a,b) and ρ (c,d) using 4polar-STORM on stress fibers of a U2OS cell stained for F-actin (AF488-phalloidin). Stick orientation is based on ρ. Colors of the sticks correspond to δ (a,b) and ρ (c,d). Scale bars: 5 µm (a and c) and 500 nm (b and d). Gaussian blurring size: 39 nm. A density filter was applied to remove isolated spots. Rendering pixel size: 12.42 nm (b,d), 24.86 nm (a, c).

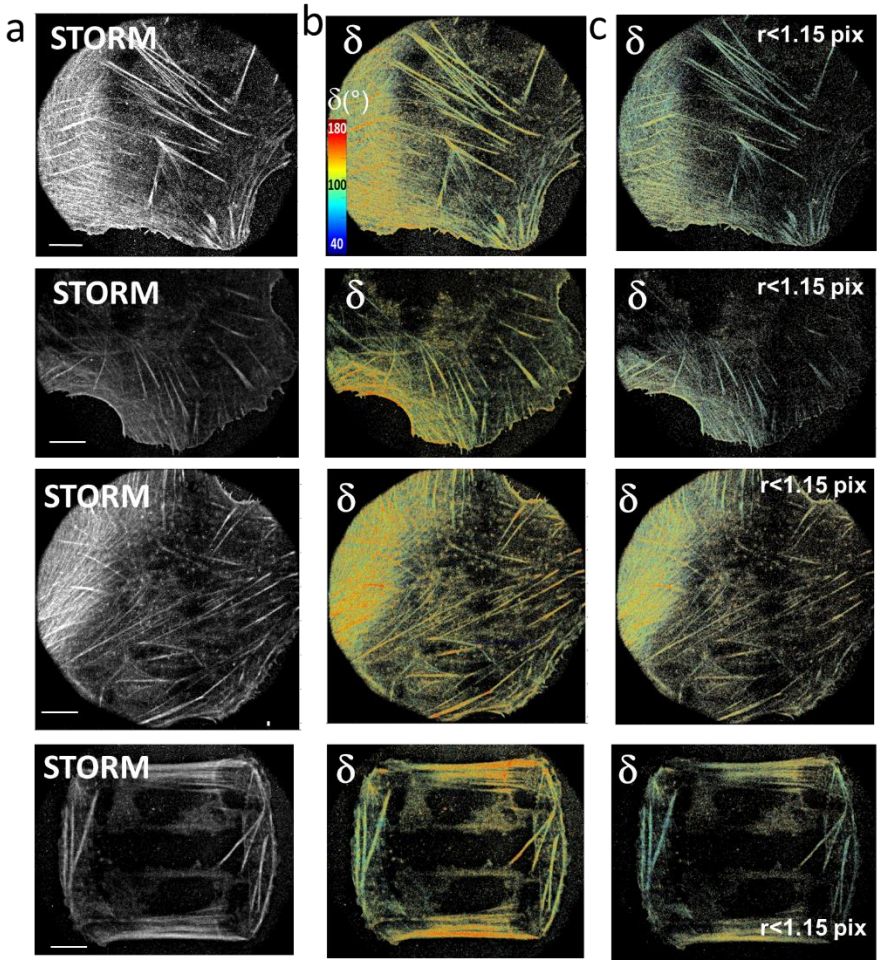

Figure S4. 4polar-STORM δ images of F-actin in fixed U2OS cells labelled with AF488-phalloidin. (a) STORM images. (b) Corresponding δ images with no thresholding of the detection parameters. (c) Corresponding δ images keeping only molecules for which the PSF radius r is below 1.15 pixels (~150 nm). δ color scales are the same for all images. Scale bars 6.5 μm.

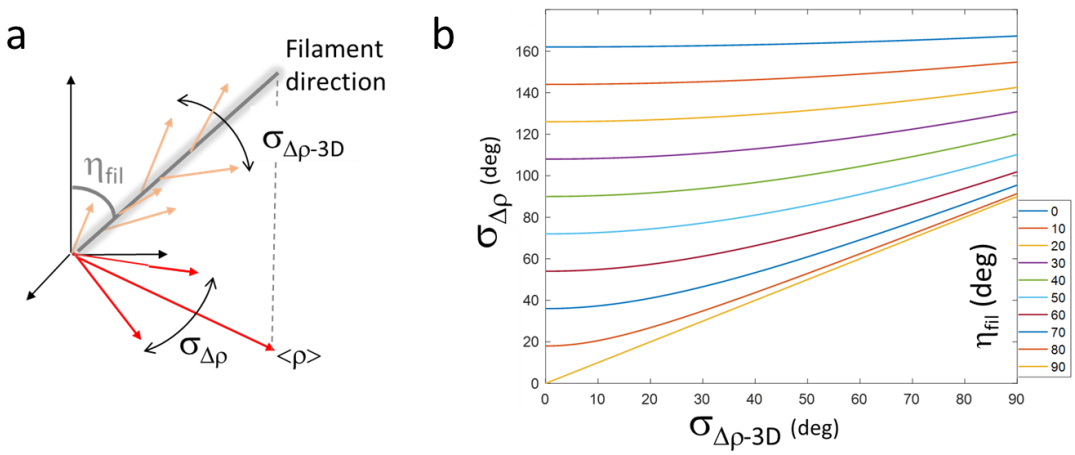

Figure S5. Retrieval bias on $\sigma_{\Delta\rho}$. (a) Schematic representation of an actin filament tilted off-plane by an angle η_{fil}, with a distribution of single molecule orientations represented by $\sigma_{\Delta\rho\text{-}3D}$. The measured distribution of projected orientations in 2D is represented by $\sigma_{\Delta\rho}$. (b) The graph shows the measured $\sigma_{\Delta\rho}$ as a function of the true value $\sigma_{\Delta\rho\text{-}3D}$, for different filament off-plane angles η_{fil}. This calculation is derived from purely geometrical considerations, considering cone apertures projected in the sample plane after a rotation is applied to them to simulate off-plane tilt.

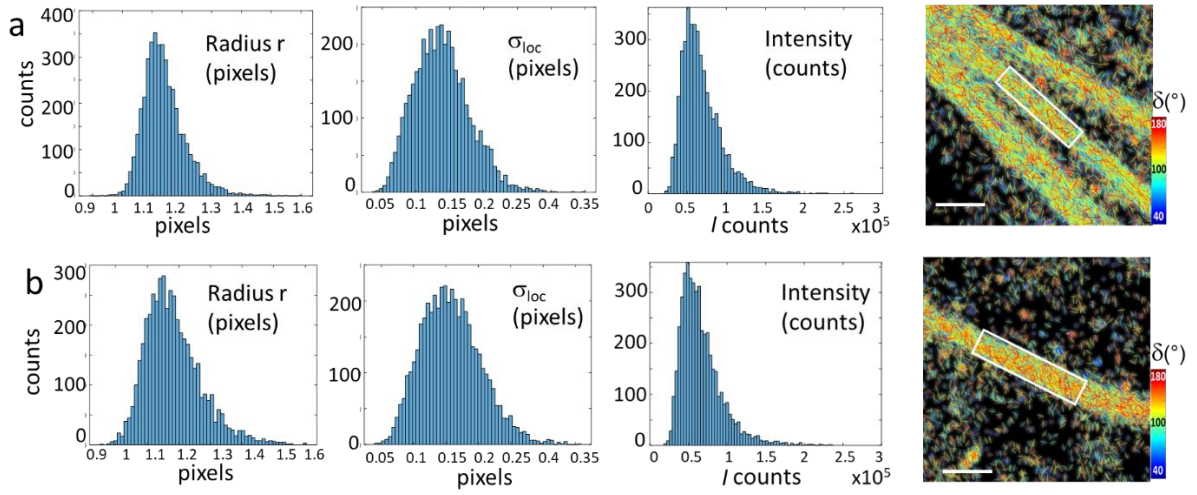

Figure S6. Statistics on detection parameters in 4polar-STORM imaging of F-actin in stress fibers in cells. Histograms of the detection parameters in different types of stress fibers in U2OS cells labelled with AF488-phalloidin (shown as δ stick images). The histograms depict values measured for all molecules present in the regions of interest shown as white rectangles. (a) In-plane ventral SF region. (b) Focal adhesion region, for which the distributions of the radius r and localization precision σ_{loc} become wider. Scale bars: 800 nm.

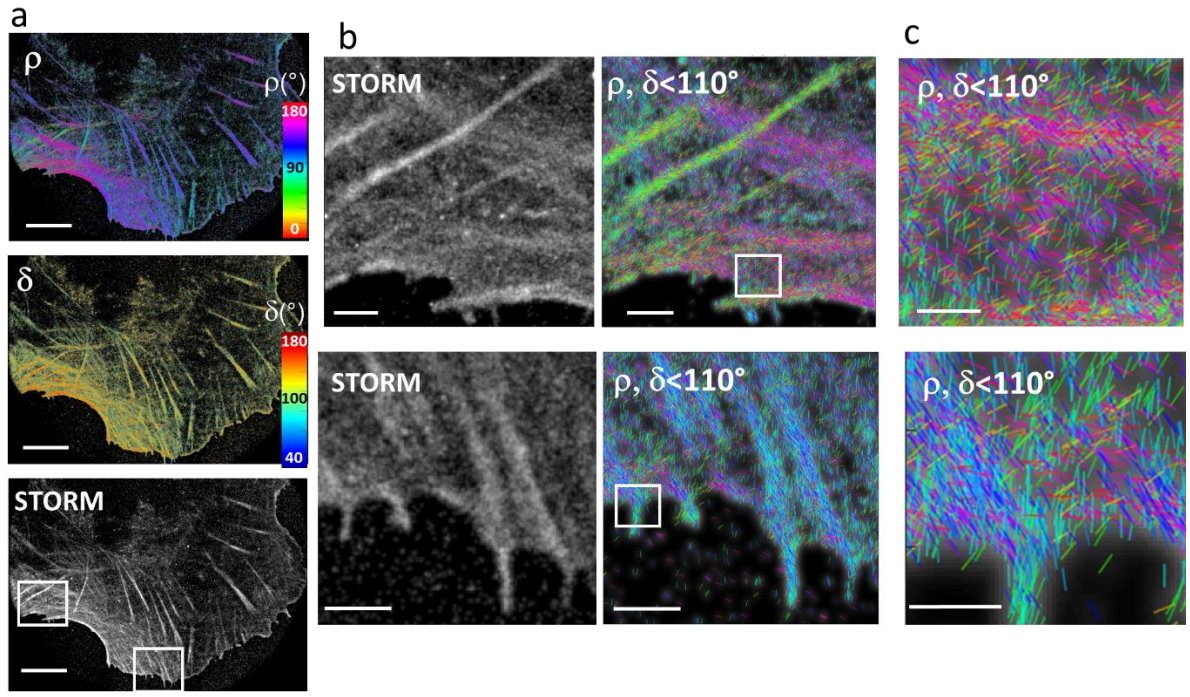

Figure S7. 4polar-STORM imaging of F-actin in cells, selecting in-plane actin filament populations. (a) Large field of view images of ρ and δ sticks as well as the corresponding single molecule localization STORM image of a U2OS cell labelled with AF488-phalloidin. (b) zoomed regions (see squares in (a)) depicting STORM and ρ-stick images for in-plane molecules only (δ < 110°). (c) stronger zoom (see squares in (b)) depicting ρ sticks for in-plane molecules only (δ < 110°). Scale bars (a) 6.5 μm; (b) 1.3 μm; (c) 500 nm.

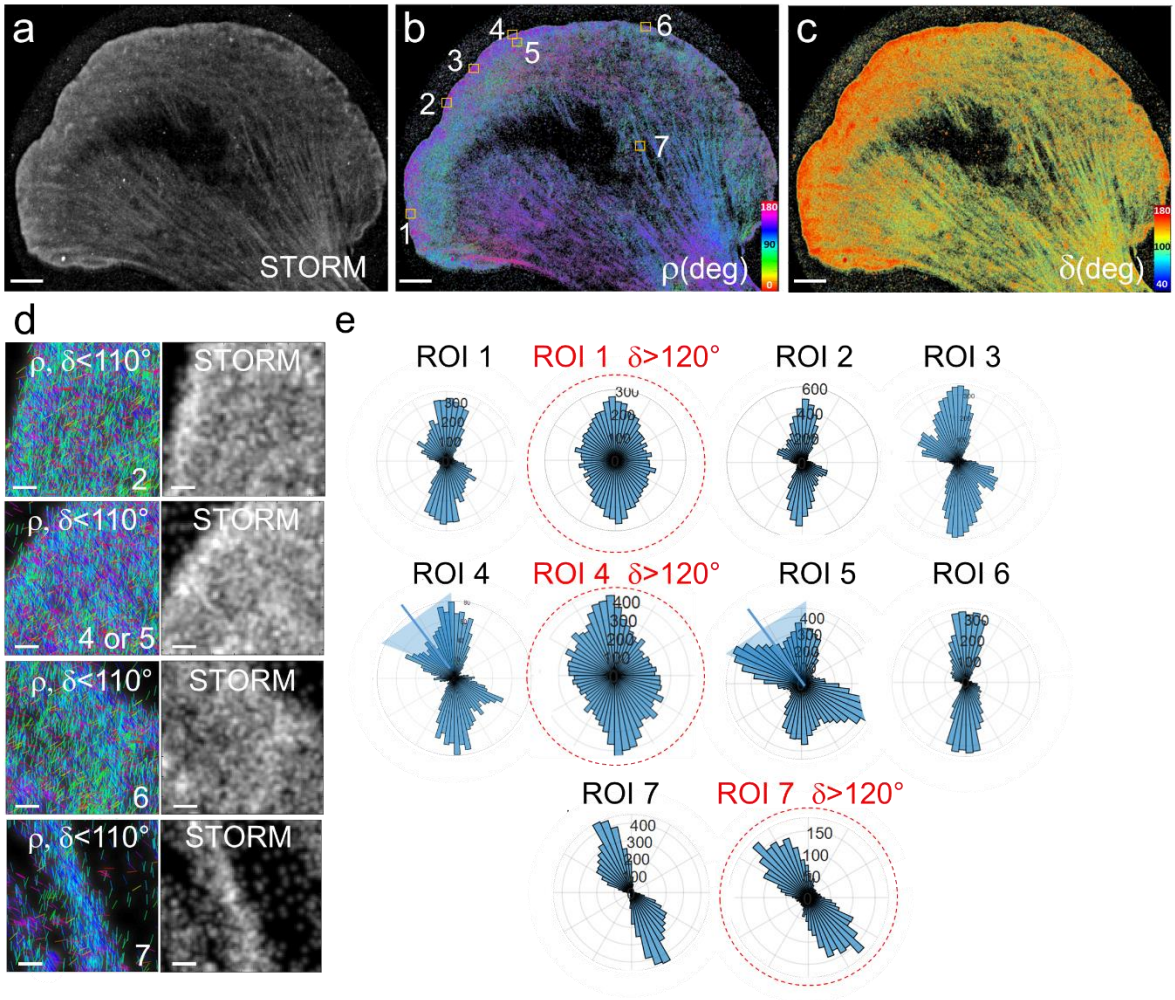

Figure S8. 4polar-STORM imaging of actin filament organization in lamellipodia. (a) Single molecule localization STORM image of a B16 cell labelled with AF488-phalloidin. (b) Corresponding 4polar-STORM ρ stick image with color-coded orientation measurements. (c) 4polar-STORM δ stick image with color-coded wobbling angle measurements. (d) Examples of ρ stick images showing molecules with $\delta < 110°$ and corresponding STORM images in selected ROIs (squares in (b)). ROIs 1-6, regions in the lamellipodium; ROI 7, SF. (e) Polar-plot histograms of ρ for the regions shown in (b). The condition $\delta < 110°$ is used, except for red-circled histograms for which $\delta > 120°$ molecules are selected. Scale bars (a-c), 4 μm; (d), 260 nm.

Supplementary Information References

1. Backer, A. S. & Moerner, W. E. Determining the rotational mobility of a single molecule from a single image: a numerical study. *Opt. Express* **23**, 4255 (2015).

2. Forkey, J. N., Quinlan, M. E. & Goldman, Y. E. Protein structural dynamics by single-molecule fluorescence polarization. *Prog. Biophys. Mol. Biol.* **74**, 1–35 (2000).

3. Axelrod, D. Chapter 7 Total Internal Reflection Fluorescence Microscopy. *Methods in Cell Biology* vol. 89 169–221 (2008).

4. Petrov, P. N., Shechtman, Y. & Moerner, W. E. Measurement-based estimation of global pupil functions in 3D localization microscopy. *Opt. Express* **25**, 7945–7959 (2017).

5. Yan, T., Richardson, C. J., Zhang, M. & Gahlmann, A. Computational correction of spatially variant optical aberrations in 3D single-molecule localization microscopy. *Opt. Express* **27**, 12582 (2019).

6. C. R. Cantor and P. R. Schimmel. *Biophysical Chemistry. Part II: Techniques for the Study of Biological Structure and Function*.

7. Brasselet, S. Polarization-resolved nonlinear microscopy: application to structural molecular and biological imaging. *Adv. Opt. Photonics* **3**, 205 (2011).

8. Axelrod, D. Carbocyanine dye orientation in red cell membrane studied by microscopic fluorescence polarization. *Biophys. J.* **26**, 557–573 (1979).

9. Ding, T., Wu, T., Mazidi, H., Zhang, O. & Lew, M. D. Single-molecule orientation localization microscopy for resolving structural heterogeneities between amyloid fibrils. *Optica* **7**, 602 (2020).

10. Valades Cruz, C. A. *et al.* Quantitative nanoscale imaging of orientational order in biological filaments by polarized superresolution microscopy. *Proc. Natl. Acad. Sci. U. S. A.* **113**, (2016).

11. Backlund, M. P., Lew, M. D., Backer, A. S., Sahl, S. J. & Moerner, W. E. The role of molecular dipole orientation in single-molecule fluorescence microscopy and implications for super-resolution imaging. *ChemPhysChem* **15**, 587–599 (2014).

12. Sergé, A., Bertaux, N., Rigneault, H. & Marguet, D. Dynamic multiple-target tracing to probe spatiotemporal cartography of cell membranes. *Nat. Methods* (2008) doi:10.1038/nmeth.1233.

13. Pengo, T., Holden, S. J. & Manley, S. PALMsiever: A tool to turn raw data into results for single-molecule localization microscopy. *Bioinformatics* **31**, 797–798 (2015).

14. Botev, Z. I., Grotowski, J. F. & Kroese, D. P. Kernel density estimation via diffusion. *Ann. Stat.* **38**, 2916–2957 (2010).